

Phosphoric Acid Doped Polybenzimidazole-Based Membrane Electrode Assembly for a Highly Sensitive and Selective Acetone Gas Sensor

by

Timothy Cumberland

A thesis

presented to the University of Waterloo

in fulfillment of the

thesis requirement for the degree of

Master of Applied Science

in

Chemical Engineering

Waterloo, Ontario, Canada, 2018

© Timothy Cumberland 2018

Author's declaration

I hereby declare that I am the sole author of this thesis. This is a true copy of the thesis, including any required final revisions, as accepted by my examiners.

I understand that my thesis may be made electronically available to the public.

Abstract

The increase in demand for small, inexpensive and portable gas sensors, which are sensitive and reliable, have generated much of the research interest toward solid oxide metal-based acetone gas sensors. However, despite the numerous improvements made to these devices, issues such as high energy consumption, poor sensitivity and selectivity have hindered their advance to the commercial stage. Medium to high temperature fuel cells have been studied extensively. Thus, this represents an opportunity to capitalize on the opportunity to design a new sensor technology that can circumvent some of the disadvantages inherently found in solid oxide sensors. This work is based on a proof-of-concept phosphoric acid doped polybenzimidazole (PBI)-based fuel cell acetone gas sensor as a potential alternative to the current solid metal oxide sensors. The fuel cell sensor was fabricated from commercially available membrane electrode assembly (MEA) and PBI membranes. Both solid and porous PBI membrane morphologies were studied in detailed to explore their ion conductivity and their effects on the sensor performance.

Porous PBI membranes were found to have superior ion conductivity in terms of thickness, acid doping concentration and temperature over the solid membrane. MEAs fabricated from these membranes were evaluated as sensors for acetone gas. The porous PBI membranes with thickness of 100-105 μm , acid doping with 5M H_3PO_4 and operated at 140°C were found to have the best sensing characteristics over a parameter range of 15 - 200 μm , 100 - 180°C, 2 - 10 M H_3PO_4 . Higher sensor response was obtained at 180°C but the MEA's mechanical integrity was severely compromised. Sensitivity analysis on an optimized sensor revealed a linear relationship between the sensor response and acetone concentration that was valid over a wide range of acetone concentrations. This is a desirable property that current solid oxide sensors cannot yet achieve. The sensor also had comparable selectivity to that of solid oxide sensors for other volatile gases. However, due to the commercial nature of the catalyst and its low catalyst loading, the detection of the fuel cell sensor was within the range of 15-20 ppmv. Overall, the proof-of-

concept showed potential with many proposed improvements to enhance the catalyst activities and selectivity over that currently available.

Acknowledgements

I would like to thank my supervisor Professor Aiping Yu and Professor Zhongwei Chen for providing the necessary resources to make this research project possible. I am very grateful for the opportunity to work on a very applied, commercially related problem.

I am deeply thankful to Dr. Gaopeng Jiang for his continuous guidance. Without his vast knowledge and familiarity with the project, much of this work would not have been possible. I would also extend my gratitude to Jared Lenos, who guided me in the initial phase of the project and provided the testing system framework for me to build upon. Furthermore, I appreciate the invaluable advice from the sensor team members: Abel Sy, Zhang Jing and Stefan Delaat.

I also want to thank Bert Habicher and Richard Hecktus for their resourcefulness when it came to the mechanical designs and set up.

Lastly, I would like to thank my parents for their continuous encouragement and support throughout my undergraduate, as well as my graduate school journey.

Dedication

To my parents, Hannah and Michael, who always provide an ocean of love and encouragements. Without their support, I would have never had the opportunity to go this far.

Table of Contents

Author's declaration	ii
Abstract.....	iii
Acknowledgements	v
Dedication	vi
List of Figures	x
List of Tables	xii
1. Introduction.....	1
1.1. Gas Sensors for Acetone Detection.....	1
1.2. Fuel Cell Gas Sensor	4
1.3. Characteristics of an Ideal Gas Sensor	5
1.4. Research Objectives.....	5
1.5. Organization of Thesis.....	6
2. Phosphoric Acid Fuel Cell for Acetone Gas Sensor.....	7
2.1. Why Phosphoric Acid Fuel Cell?.....	7
2.2. Principle of Operation.....	9
2.3. Polybenzimidazole Membrane	10
2.4. Catalyst.....	12
2.5. Electrode Membrane Assembly	13
3. Material and Methods.....	15
3.1. Materials.....	15
3.1.1. Membrane Synthesis and Doping.....	15

3.1.2.	Gas Diffusion Electrode.....	20
3.1.3.	Membrane Electrode Assembly Fabrication.....	21
3.2.	System Design.....	22
3.2.1.	Sensor Housing Design.....	22
3.3.	Fuel Cell Sensor Testing	28
3.3.1.	Fuel Cell Test Set-up.....	28
3.3.2.	Sensor Response Curve and Data Analysis	34
3.3.3.	Experiment Outline.....	37
4.	Results and Discussion	38
4.1.	Sensor Housing Design	38
4.2.	Membrane Synthesis and Characterization.....	39
4.2.1.	Membrane Synthesis	39
4.2.2.	Membrane Characterization	42
4.3.	MEA Fabrication.....	50
4.4.	Sensor Performance and Optimization	51
4.4.1.	Thickness.....	51
4.4.2.	Acid Doping Concentration	53
4.4.3.	Temperature	55
4.4.4.	Sensitivity, Detection Limit and Selectivity	57
5.	Conclusions and Recommendations	62
5.1.	Summary	62
5.2.	Recommendations	63
	References	65

Appendices.....	77
Appendix A: Estimation of Analyte Vapour Concentration with Henry's Law	77
Appendix B: Fuel Cell Sensor Housing Design Drawing	79
Appendix C: Test Automation and Data Analysis Code.....	83
DMM Controller and Data Acquisition	83
Hardware Control Script.....	83

List of Figures

Figure 1-1: Schematic of Gas Sensors' Topography	1
Figure 1-2: Types of gas Sensors	2
Figure 2-1: PAFC Operation with Acetone	10
Figure 2-2: PBI Structure and Complexation with Phosphoric Acid	12
Figure 2-3: Fundamental Construction of MEA	14
Figure 3-1: Custom Casting Plate for PBI Membrane Synthesis.....	16
Figure 3-2: sPBI and pPBI Synthesis and Acid Doping Procedure up to MEA fabrication.....	17
Figure 3-3: Through-plane 3D Design and Pt foil and Membrane Layout	19
Figure 3-4: MEA Hot Press Condition and GDE Alignment	21
Figure 3-5: Phosphoric Acid Storage Chamber for MEAs.....	22
Figure 3-6: MEA Containers Design. Left: gas analyte travel part; dimensions are in cm.....	24
Figure 3-7: 3D-rendered Heat Element for Inside Implementation.....	25
Figure 3-8: Left: As made PTFE Housing; Right: Set-up before Operation.....	26
Figure 3-9: 3D-rendered Heat Element Outside Implementation	27
Figure 3-10: Left: As made PEEK Housing; Right: Set up before testing	28
Figure 3-11: One Sensor Test Cycle Operation Timing of Different Components	31
Figure 3-12: Two-relay Module Wiring and Set-up.....	31
Figure 3-13: Schematic Overview of the Fuel Cell Test Set-up.....	32
Figure 3-14: Fuel Cell Test-up During Operation.....	33
Figure 3-15: Typical Fuel Cell Sensor Response Curve and Key Characteristics	34
Figure 4-1: sPBI Membranes with Uneven PBI Distribution	39
Figure 4-2: As-Made sPBI (left) and pPBI (right) Membranes After Recovery.....	41
Figure 4-3: PBI Resin Weight vs. Thickness of the Membrane for sPBI and pPBI.....	42
Figure 4-4: Effect of Thickness on Conductivities of sPBI and pPBI Membranes at an the Acid Doping Concentration of 5M H ₃ PO ₄ and the temperature of 140°C	43

Figure 4-5: Through-plane Conductivities of sPBI and pPBI versus the Acid Doping Concentration; Membrane Thickness = 100um, Anhydrous, Temperature = 140°C.....	45
Figure 4-6: Through-plane Conductivities of sPBI and pPBI versus the Temperature; Membrane Thickness = 100um, Anhydrous, Acid Doping Concentration = 5M	46
Figure 4-7: Cross-section SEM Images of sPBI and pPBI Membranes.....	49
Figure 4-8: As-Made MEA from a sPBI Membrane with a quarter for size comparison.....	50
Figure 4-9: Fuel Cell Sensor Performance for 620ppm Acetone; Acid Doping Concentration = 5M, Temperature = 140°C.....	51
Figure 4-10: Fuel Cell Sensor Performance at 620ppm Acetone; Membrane Thickness = 100 - 105um, Temperature = 140°C.....	53
Figure 4-11: Fuel Cell Sensor Performance at 620ppm Acetone; Membrane Thickness = 100 - 105um, Acid Concentration = 5M H ₃ PO ₄	55
Figure 4-12: MEA Condition After Testing at 140°C (right) and 180OC (left); Membrane Thickness = 103um.....	56
Figure 4-13: Sensitivity Study of the 100um sPBI and pPBI MEA at 140°C; Acid Doping Concentration = 5M. Left: Response Curves; Right: Linearity	57
Figure 4-14: Low Acetone Concentration Sensor Reponses with sPBI and pPBI	59
Figure 4-15: pPBI and sPBI Sensor Reponse for Acetone, Ethanol and Methanol at 600ppmv	61

List of Tables

Table 1-1: Summary of Recent Literatures SMO Gas Sensors	3
Table 1-2: Advantages and Disadvantages of SMO Gas Sensors	3
Table 3-1: Comparison Between the Inside and Outside Position for Heating Element	23

1.Introduction

1.1. Gas Sensors for Acetone Detection

Gas sensors are devices capable of providing quantitative measurements and information about a specific chemical present in the sampled gas. A gas sensor is comprised of two main components: a transducer and an active layer [1]. The active layer converts the chemical information to measurable electrical or other signals based on the property changes induced by the detected chemical. The transducer filters, amplifies and outputs the signals to external data collecting devices, where it is further processed into meaningful information. Figure 1-1 provides an overview of this description.

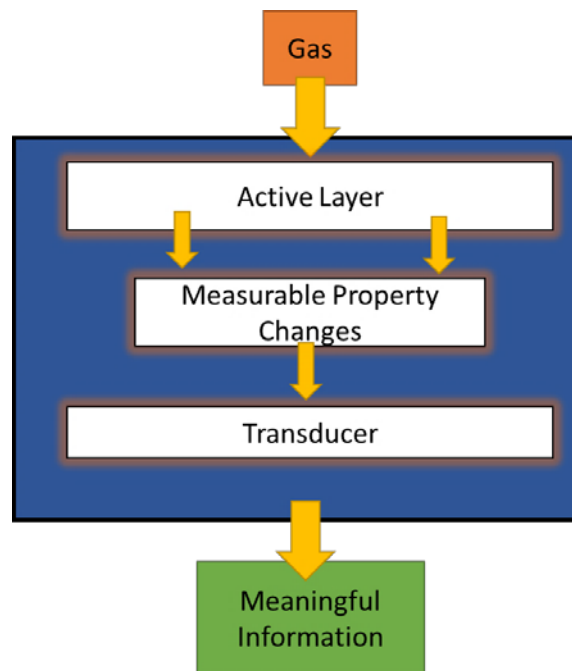


Figure 1-1: Schematic of Gas Sensors' Topography

The interest in developing smaller, more reliable, and lower power requirement gas sensors has grown in the recent years to their wide range of applications. Acetone gas sensors have recieved a significant amount of attention due to its utility in environmental monitoring, food packaging, quality control, production safety, medical and healthcare related to diabetes and cancer diagnosis [1]–[5].

Many types of acetone gas sensors have been explored. In general, these technologies are segmented into two main categories: non-electrical signal and electrical signal. Figure 1-2 shows a breakdown of each sensor technology under these two main categories [1], [2].

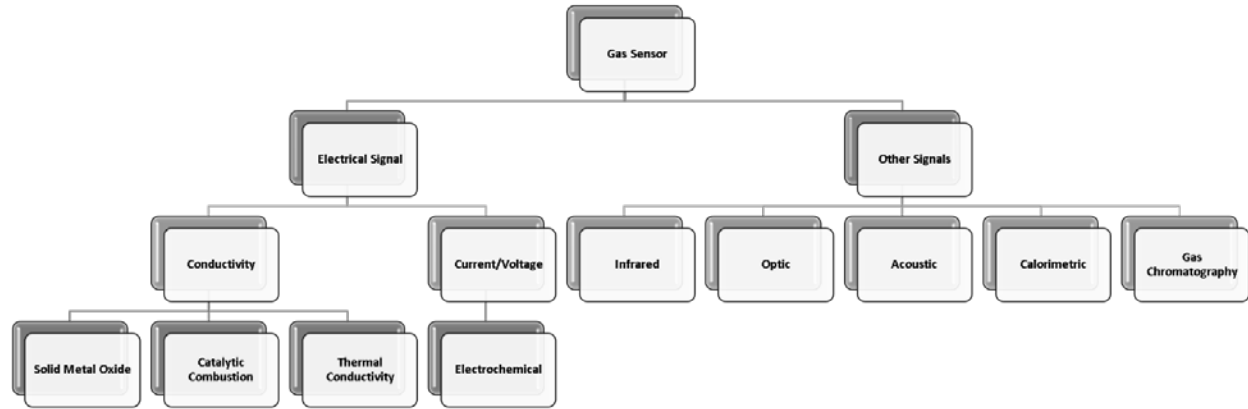


Figure 1-2: Types of gas Sensors

For gas sensors, solid metal oxides (SMO) are the most researched and investigated type. SMO gas sensors, also called chemoresistive sensors work on the principle of surface adsorption followed by catalytic oxidation of the sample gas. This results in a change in the adsorbent electrical resistance. Moreover, the magnitude of the change in the resistance is correlated to the concentration of the sample gas. The details on SMO and other technology working principles are not within the scope of this work and can found elsewhere [1], [2], [5].

The active materials in SMOs are usually single, binary or composite metal oxides, either as a bulk or as a thin layer. The most promising direction for active material research is for binary metal oxides decorated with noble metal particles, which have shown to enhance the catalytic sensitivity and selectivity. Table 1-1 summarizes the recent literature involving SMO gas sensors for acetone.

Table 1-1: Summary of Recent Literatures SMO Gas Sensors

SMO morphologies	Detection Limit	Testing Environment	Operating Temperature (°C)	Reference
Co-doped ZnO nanofibers	5 ppm	25% RH	360	[6]
In ₂ O ₃ -coated CeO ₂ nanoclusters	500 ppb	80% RH	450	[7]
Zn ₃ N ₂ /ZnO hollow microspheres	70 ppb	90% RH	200	[8]
Pt-WO ₃ hemitube	120 ppb	85% RH	300	[9]
Pt-dope SnO ₂ NFs	25 ppb	80% RH	300	[10]
Au/1D α-Fe ₂ O ₃	1 ppm	45% RH	270	[11]
Si-doped WO ₃	20 ppb	90% RH	400	[12]
PtO ₂ -SnO ₂ nanofibers	0.6 ppm	95% RH	400	[13]
Fe-C-WO ₃ walnut-like particles	0.2 ppm	90% RH	300	[14]
W-NiO flower-like spheres	0.1 ppm	--	250	[15]
In ₂ O ₃ -reduced GO nanocubes	5 ppm	50% RH	225	[16]

From Table 1-1, one can see that a wide variety of SMO materials have been investigated to varying degrees of success in terms of the detection limit. However, substantial discrepancy exists amongst these studies in terms of performance and testing conditions. Table 1-2 summarizes the general advantages and disadvantages from these studies and other sources [2][5][17].

Table 1-2: Advantages and Disadvantages of SMO Gas Sensors

Advantages	Disadvantages
Simple sensor fabrication	Complex material synthesis
Ease of use	High energy consumption
Compatible with microelectronics	Mass production issues
Low detection limit	Sensitivity, selectivity
Reliability	Environment sensitive (RH)

Despite the advantages of SMO gas sensors, their disadvantages severely hinder progress toward commercialization. The low sensitivity and selectivity of SMO gas sensors are a major issue. Due to the indirect nature of its sensing mechanism, other gases and humidity can easily

interfere with the signal. The low detection limits reported in Table 1-1 apply to pure acetone in air or other inert media. As a result, strategies such as combining two or more SMOs and/or decorating the SMOs with noble metal nanoparticles have proven to mitigate this drawback. However, the added complexity and cost to the material synthesis creates more challenges for commercialization although sensor fabrication is simple once the active materials are prepared. Energy consumption is also a major concern. At an operating temperature as high as 450°C, an energy source is needed to constantly power the device. The use of smaller active material area will lower overall energy consumption, but it will also lower sensor sensitivity. Finally, other concerns such as non-linear response profiles and signal drift as the material ages also pose difficulties for producing reliable and long-lasting sensors [18] [19]. These issues further limit SMO gas sensors' capabilities in practical applications.

1.2. Fuel Cell Gas Sensor

To address these inherent disadvantages, another alternative is considered: electrochemical or fuel cell gas sensors. Contrary to SMO sensors, fuel cell gas sensors have proven to be very successful at a commercial level. The prime example of this is the alcohol breathalyzer. Fuel cell-based alcohol breathalyzers are the gold standard for detecting breath alcohol in law enforcement. Compared to SMO alcohol breathalyzers, fuel cell sensors are alcohol-specific, which make them more accurate and reliable. The only disadvantage is the cost associated with the use of a noble metal catalyst within the electrodes [19]-[21]. However, the addition of noble metal particles into the synthesis process of state-of-the-art SMO gas sensors has drastically increased their cost and complexity.

In this work, a proof-of-concept for a phosphoric, acid-doped, polybenzimidazole-based (PA-PBI) MEA for a fuel cell that can detect acetone gas will be presented. Compared to Nafion-based fuel cells, a PA-PBI-based fuel cell offers several advantages: (1) higher acetone oxidation kinetics due to higher possible operating temperature, (2) improved catalyst poisoning tolerances, (3) complete circumvention of water and temperature management, (4) cheaper and

better, and chemical and physical stability than Nafion, and (5) simplification of fuel cell design [22][23]. The last point is arguably the most important since a simpler and smaller design will promote more applications for the sensor. Further discussion of the reason for selecting a PA-PBI-based fuel cell will be given in Chapter 2, as well as an overview of the mechanism and operation in sensing application.

1.3. Characteristics of an Ideal Gas Sensor

Gas sensors, which work on scientific principles, have ideal characteristics. These characteristics are defined by the application and purpose of the sensor. Factors such as size, temperature, pressure, humidity and the complexity of the sample matrix are used as benchmarks to determine the suitability of a sensor for a certain application. In general, an ideal gas sensor should have the following characteristics [24]:

- Reliability and stability of sensor response with no hysteresis
- Short response time and recovery time
- High signal-to-noise ratio
- High selectivity to the analyte
- High sensitivity on the analyte concentration

1.4. Research Objectives

This research project aims to explore a different alternative to the acetone gas sensor technology, namely a PA-PBI based fuel cell. The work contained within this thesis will try to establish baselines and standards for a solid electrolyte fuel cell sensor on which future research can be based upon for further improvement. To this end, this work is comprised of three main objectives:

- I. Prepare a prototype of a fuel cell acetone gas sensor with commercially available catalyst and assess its performance and feasibility.

- II. Study the solid electrolyte material and PBI, to explore and optimize the factors affecting the sensor performance
- III. Develop a standard testing platform for electrochemical gas sensor characterization, capable of evaluating different sensor prototypes and different testing conditions using a standardized procedure and performance analysis.

1.5. Organization of Thesis

This thesis contains four chapters following Chapter 1. Chapter 2 briefly introduces the working principles of a phosphoric acid fuel cell and the reaction mechanism for oxidizing acetone. Chapter 3 describes the preparations and fabrication of different components of the sensor. Furthermore, Chapter 3 will also discuss the design and development of the sensor structure, data acquisition system and automation of data analysis. Finally, Chapter 3 will conclude with the test procedure, experimental plan and data analysis techniques that were used to assess the sensors. Chapter 4 will present the results from the experimental plan outlined in Chapter 3. Detailed analyses and discussions will be provided to assess the solid electrolyte, sensor performance and effectiveness of the data acquisition system. The final chapter will summarize the entire study and provide recommendations for future work.

2. Phosphoric Acid Fuel Cell for Acetone Gas Sensor

2.1. Why Phosphoric Acid Fuel Cell?

A very limited amount of literature exists on the use of fuel cells as an acetone sensors. However, enough has been done to select an appropriate technology for further research. Haverhals showed that proton exchange membrane fuel cells (PEMFC) can provide a response to acetone in his PhD thesis [25]. Haverhals used a Nafion® membrane with a carbon-based, platinum (Pt)-supported catalyst. However, these sensors lacked stability due to the decrease in the proton conductivity at very low humidity. While having excellent chemical and electrochemical stability, Nafion® membranes only operate at relatively low temperatures (<80°C) and have high crossover. In addition, the membranes must be kept hydrated throughout their operation; without proper hydration, Nafion® membrane conductivity decreases drastically. In low temperature PEMFCs, the Pt catalyst is susceptible to poisoning by trace amounts of CO, which will significantly decrease the fuel cell performance. In addition to these drawbacks, Pt and Nafion® are very expensive materials, which make the cost associated with producing such devices on a larger scale impractical [26].

Most recently, Bhansali et al. [21] designed a three-electrode fuel cell in a miniaturized form to detect acetone gas for non-invasive diabetes monitoring. The solid electrolyte used in this study was a Nafion 115 membrane. While the fuel cell displayed good response and low detection limit (0.5 ppmv), the sensitivity of the sensor was poor. A hypothesis test revealed that the responses at the 0.5, 1, and 2ppmv levels not statistically different from each other. This was detrimental to its application in diabetes monitoring because this increased the probability of making a Type I error when preparing a diagnosis. The use of a Nafion membrane is also disadvantageous due to fuel crossover and mechanical swelling, which will degrade the membrane electrode assembly (MEA) and consequently, its effective lifetime [26]. The sensor also operated at room temperature without any temperature or humidity control. This operating

condition was not ideal for a normal Nafion-based fuel cell, and therefore hindered its performance [27].

Strict control on hydration and humidity is undesirable for sensors because hydration can only be kept at steady state after start-up when fuel cells are used as power source,. However, when fuel cells are used as sensors, the uses are intermittent. The hydration of the membrane will be delayed at each start-up and will affect the long-term operational stability of the device due to the accumulation of thermal and physical cycle stress. Moreover, another problem occur when the fuel cell operates below 100°C. At these temperatures, water exists in two phases: vapour and liquid. If the temperature and humidity is mismanaged within the cell, it can lead to flooding from the condensed water vapour. This further complicates the design of fuel cell sensors.

While the operation principle and mechanism of a phosphoric acid fuel cell (PAFC) is similar to that of a PEMFC, one distinct difference distinguishes PAFCs: the acid-doped membrane. Low temperature PEMFCs mostly use perfluoro-sulfonic acid (PFSA) membranes (e.g. Nafion®) soaked or humidified with water to conduct protons. This only allows the fuel cell to operate up to a temperature of 80°C. In comparison to PEMFCs, the solid electrolyte membrane of PAFCs is soaked or doped with concentrated phosphoric acid instead of water. This allows PAFCs to operate at higher temperatures ranging from 120-180°C [28][29]. Many studies have shown that the likelihood of CO poisoning on the catalyst is greatly reduced at higher temperatures. At this increased operating temperature, the platinum catalyst can tolerate up to 3% CO contaminant in the input fuel [30], [31].

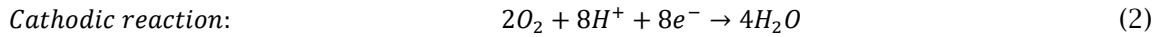
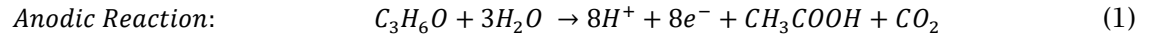
Thus, when approaching the fuel cell sensor design, a PAFC is more appropriate. At higher temperatures, the kinetics of the oxygen reduction at the cathode will also improve. In turn, this enables quicker sensor response time. Water produced from the cathode will only be present in the pure vapour state, and thereby avoid the flooding problem in the cell. Water and heat management are not a concern in the design of the control and sensing system. To summarize,

PAFC has enormous advantages over the low temperature PEMFC in terms of design and operation management.

2.2. Principle of Operation

PAFCs are designed and operated similarly to other fuel cells. PAFCs are generally fabricated from an anode, cathode and a solid electrolyte as the main components. The anode and cathode serve as the current collector and catalyst support. The interface between the surface of the cathode/anode and solid electrolyte is usually coated with the catalyst where the electrochemical reactions occur. During operation, electrons produced at the anode are transported through an external circuit to the cathode where the electrons are consumed by the cathodic reaction. Simultaneously, the solid electrolyte or proton exchange membrane (PEM) conduct the protons from the anode to the cathode and serve as a separator to prevent the flow of electrons. Carbon paper or carbon cloth, are the material of choice for the conductive cathode/anode material as they permit relatively fast gas diffusion while having a large surface area to support the catalyst [32].

For this application, the gaseous acetone acts as fuel for the cell. Acetone is oxidized at the anode to produce acetic acid and carbon dioxide. At the cathode, oxygen is simultaneously reduced to water [21]. Figure 2-1 illustrates construction and operation of a PAFC with acetone. The anodic and cathodic reactions are shown below:



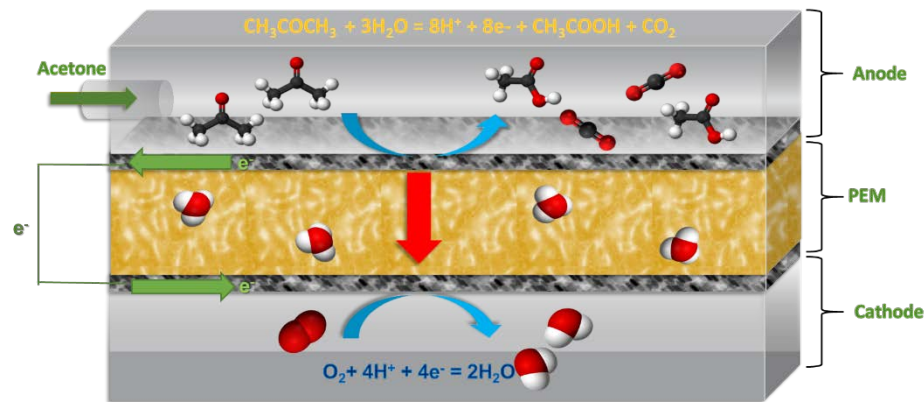


Figure 2-1: PAFC Operation with Acetone

2.3. Polybenzimidazole Membrane

Due to the involvement of acid within the electrolyte and elevated operating temperatures, a solid electrolyte for a PAFC should satisfy the following conditions:

- High ionic conductivity
- High chemical stability
- High mechanical strength and temperature gradient stress tolerance
- Humidity tolerance
- Low fuel cross-over

In the search for the ideal membrane material, researchers have investigated many polymers as candidates for PAFC. As a result of this search, polybenzimidazoles (PBI) emerged as the best candidate [33]–[35]. PBI is an inexpensive polymer invented by Carl Shipp Marvel [36]. Due to its high stability, it was used as coating for firefighting and astronaut protective equipment. An acid-doped PBI membrane retains good mechanical properties, excellent thermal stability and high conductivity even under anhydrous conditions [29], [37], [38]. The proton conductivity of doped PBI can be further increased by increasing the acid concentration during doping. However, the tradeoff is that the presence of excess free acid will degrade the mechanical strength of the membrane [32]. When the acid doping level is optimized, the proton conductivity

of PBI membrane can be very promising. The reactive sites (=N-H) and acidic anions contribute to the proton transfer through the extensive hydrogen bond network. Higher operating temperatures will also promote the proton transfer within the electrolyte. At temperatures from 120°C to up to 200°C, proton conduction follows the Grotthus mechanism. This mechanism involves the displacement of hydrogen bonds by additional hydrogen protons between adjacent acid molecules. This propagates the proton across the membrane from one side to the other.

The proton conductivity of PBI membrane is closely related not only to the concentration, but also to the type of acid used during the doping process. The doped acids decrease the in the following order: $\text{H}_2\text{SO}_4 > \text{H}_3\text{PO}_4 > \text{HClO}_4 > \text{HNO}_3 > \text{HCl}$ [39]. Sulfuric acid has the best proton transfer property up to 0.2 S/cm at optimized conditions. However, its effectiveness is dependent on humidity [40]. This is not ideal for sensor applications since the system often operates at higher temperature for an extended period then is turned off for another extended period. Humidity cannot easily be maintained and controlled. Additionally, the requirement to control humidity will lead to some of the disadvantages that PEMFCs have in terms of design complexity and reliability. Phosphoric acid is the best candidate for this application due to its ability to maintain a high conductivity even in the anhydrous state. Studies have shown that fuel cells with phosphoric acid-doped PBI membranes performed remarkably

well and remained stable at 185°C under an environment containing up to 3% CO [41]. Figure 2-2 illustrates the structure of PBI and the complexation with phosphoric acid molecules.

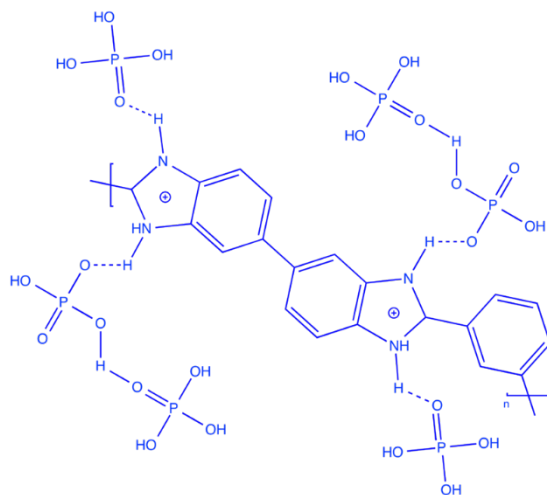


Figure 2-2: PBI Structure and Complexation with Phosphoric Acid

The membrane fabrication process, acid doping procedure, proton transport and fuel cell performances have been investigated extensively elsewhere [41]–[45]. This work will focus on the PBI membrane and how tuning different parameters such as thickness, doping concentration and temperature affect the sensor performance.

2.4. Catalyst

A large body of research exists on PAFC's catalysts. To date, Pt and Pt alloy-based catalysts are still the best options for PAFCs. Carbon-supported Pt electrode have been widely used and most thoroughly investigated for PAFCs [32]. In general, research has focused on three areas: (1) improving ORR, (2) higher CO tolerance and lower over-potential/ohmic loss, (3) enhancing durability, temperature and corrosion resistance. Most of the research efforts have been focused on improving the oxygen reduction (ORR) capability for PAFCs. Following is a brief overview.

Several Pt alloy-based materials such as Pt-Ni, Pt-Cr, Pt-Co have been investigated and found to be much more effective in reducing oxygen than carbon supported Pt [46]–[50]. A bimetallic nano-particle catalyst comprised of 3nm layer of Pt inserted into 5nm of Pd was

synthesized and evaluated by Peng et al [51]. The catalyst electrochemical properties were measured and found to have many positive properties for ORR [52] .

Carbon-supported Pt-Co nanoparticles were prepared at different atomic ratios with the goal to minimize Pt loading [53]. These catalysts, especially at Pt-Co (1:1)/C and Pt-Co (2:1)/C exhibited better performance than pure Pt/C catalyst at 160°C and 180°C. Mamlouk et al. compared different Pt alloys such as Pt-Ni, Pt-Co and Pt-Fe and found that the Pt-Ni (1:1)/C had better performance than the commercial Pt/C at 150°C [54]. CO tolerance has also been an area of interest. A bimetallic Pt-Ru catalyst was introduced by Oettel et al. [55]. The Pt-Ru catalyst was found to have higher CO tolerance and a lower over-potential than the Pt/C catalyst. Kadirgan and coworkers found superior CO tolerance and lower over-potentials when comparing Pt-Pd/C and Pt-Co/C to Pt/C on the same supporting material. Pt-Pd/C was also investigated in terms of durability versus Pt/C [52]. Oxide materials such as zirconia were also considered to improve the durability of the catalyst[56].

Since the focus of this work is to establish a proof-of-concept fuel cell sensor based on the PAFC architecture with an emphasis on studying the solid electrolyte, a commercial Pt/C catalyst that is easily obtainable will be employed to establish baselines and enable easy replications for further research.

2.5. Electrode Membrane Assembly

At the heart of a PAFC is the electrode membrane assembly (MEA). A MEA is constructed by sandwiching a PEM between two gas diffusion electrode (GDE) layers. The GDE is comprised of a gas diffusion layer (GDL), microporous layer (MPL) and finally catalyst layer (CL). A general illustration of the architecture of an MEA is shown in Figure 2-3. Two methods can be used to fabricate an MEA: catalyst-coated substrate (CCS) or catalyst-coated membrane (CCM) [56]. For CCS, the GDL is simply coated as a layer of ink which is usually comprised of a catalyst, binder and catalyst-support material. This generates a GDE and is subsequently hot-pressed onto the PEM at an elevated temperature to fabricate the MEA. The CCM method differs only in where the

ink is deposited. Instead of depositing the ink onto the GDL, the ink is deposited directly onto the membrane, then hot-pressed between two GDLs.

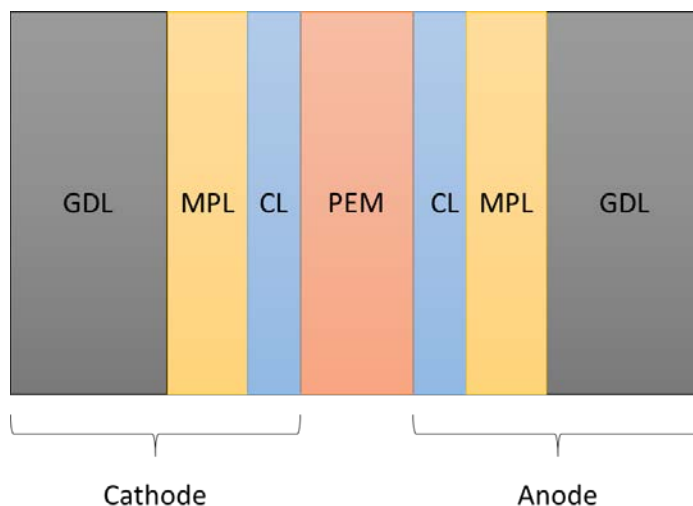


Figure 2-3: Fundamental Construction of MEA

While the CCS method is simpler, a major disadvantage is that the interfacial resistance between the GDE and membrane increases drastically due to the increased temperature accelerating the degradation of the GDE layer [57]. The CCM method yields a lower interfacial resistance due to the thinner catalyst layer and good compatibility between the catalyst layer and the membrane [57]. Notably, the most commonly used ionomer in the CCM method is Nafion®. The higher operating temperature the subsequent anhydrous or near anhydrous state poses issues to the stability of the MEA when using Nafion® as the ionomer binder [58]. Other polymer ionomers such as PTFE and PBI have been explored as potential alternatives to circumvent the inherent disadvantages of Nafion® [59], [60] .

A commercially available GDE with Pt/C catalyst is used in this research. More detailed descriptions will be provided in the Chapter 3. The use of a commercial GDE guarantees the fuel cell consistency and quickens the process of making prototypes and testing. This also leads to a reproducible process with a material that is standardized. The durability of the MEA during and after sensor testing will be qualitatively discussed in Chapter 4.

3. Material and Methods

3.1. Materials

3.1.1. Membrane Synthesis and Doping

3.1.1.1. Solid and Porous PBI membrane

To synthesize the membrane, a solution cast method is employed. This is the most common and well-studied method to produce polymeric membranes including those based on PBI [61]. All membranes were made from the same PBI resin batch (Aurorez®, 250-500um micropores) which was obtained from Hoechst Celanese (now PBI Performance Products, Inc).

To prepare a solid PBI (sPBI) membrane, the PBI resin is dissolved in N, N-dimethylacetamide (DMAc) (anhydrous, 99.8%, Sigma-Aldrich). The typical concentration of PBI in a DMAc solution is 10 - 12% w/w. The solution was stirred and heated at 70°C for at least 24 hours and then filtered to remove undissolved particulates. A custom-made casting plate (28.5 cm²) is placed inside the oven and heated to 90°C. The casting plate was made entirely from stainless steel with a special neo-ceramic glass (KW Glass System Inc.). Figure 3-1 shows the casting plate and the ceramic glass. The PBI-DMAc solution is poured into the casting plate and covered with aluminum foil. Subsequently, the casting plate is left inside the 90°C oven for at least 72 hours until the solvent is completely vaporized and only a solid PBI membrane is left behind. The membrane is left to slowly cool inside the oven. Once cooled, DI water is added to the casting plate and left to soak overnight. The water assistss with the release of the membrane from the plate glass surface. The membrane is removed using a razor blade to cut its edges and then lifting it. The membrane is then dried at 70°C overnight before further acid-doping.

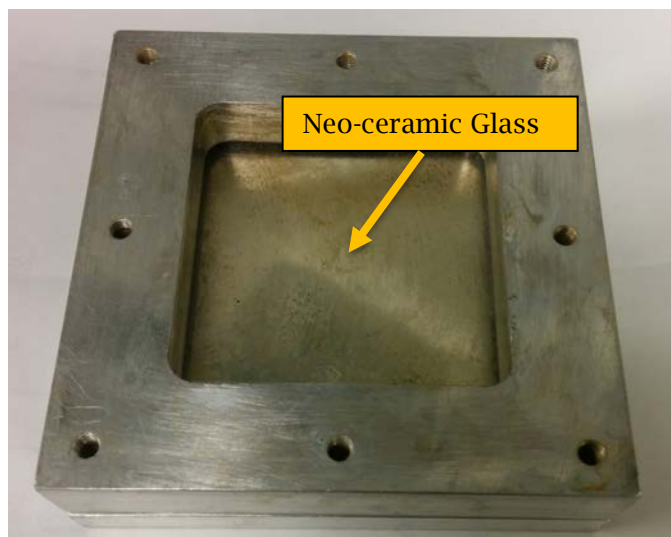


Figure 3-1: Custom Casting Plate for PBI Membrane Synthesis

To make a porous PBI (pPBI) membrane, an additional step is required. Along with the initial PBI resin, dibutyl phthalate (DBP) (99%, Sigma Aldrich) is added to DMAc. DBP is completely miscible with the PBI-DMAc solution. Well-dispersed DBP can act as porogen within the PBI matrix. After casting, the same procedure as described above is employed to recover the membrane. The membrane is then submerged into a pure methanol solution to dissolve the DBP leaving behind micropores. This process takes at least two days and requires methanol replacement every 12 hours. Lastly, the membrane is dried at 70°C overnight before acid-doping.

The thickness of the sPBI and pPBI is tuned by varying the appropriate mass of PBI used at the beginning of the process. For both morphologies, the targeted thickness range for these studies is from 20 - 200 μm . The porosity of the pPBI membrane is fixed by fixing the weight percent of DBP at 30%.

3.1.1.2. Acid doping of PBI membrane

After drying, pPBI and sPBI membranes are placed into bottles filled with H_3PO_4 (85 wt. % in H_2O , FCC, FG, Sigma Aldrich) acid at different concentrations to study the effect of doping concentration on sensor performance. Acid doping is conducted at room temperature for at least 5 days before the membrane is used to fabricate the MEA. Figure 3-2 outlines both the membrane synthesis and acid doping procedures.

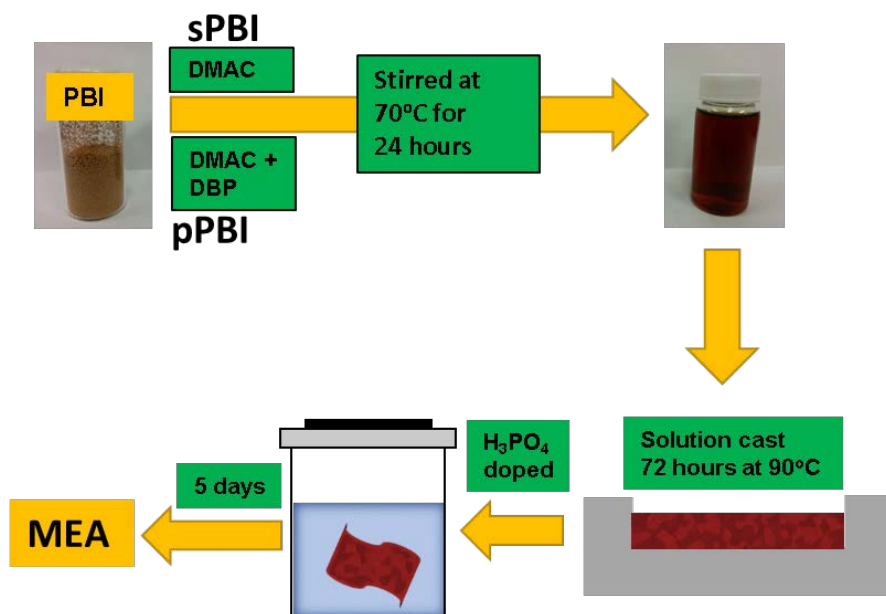


Figure 3-2: sPBI and pPBI Synthesis and Acid Doping Procedure up to MEA fabrication

3.1.1.3. Characterization Techniques

3.1.1.3.1. Electrochemical Impedance Spectroscopy

Electrochemical impedance spectroscopy (EIS) is a technique used to measure the impedance of a system. Impedance is partially analogous to an ideal resistor. However, one key difference is that impedance includes the concepts of frequency. The technique is carried out by applying an alternate current (AC) or potential across an electrochemical system and then

measuring the response in terms of current or potential. The AC or potential is usually applied as a wave. The response of an electrochemical system can be represented by Eqn (3).

$$Z(\omega) = \frac{E_0 \sin(\omega t)}{I_0 \sin(\omega t + \phi)} = Z_o (\cos \phi + j \sin \phi) = Z_{real} + Z_{img} \quad (3)$$

Eqn (3) describes the impedance Z of the system at an angular frequency ω . Z_o is the ohmic resistance of the system if the applied AC is linear or non-sinusoidal i.e. $\phi = 0$. When an AC or potential is applied at a frequency, the impedance is comprised of two parts: a real part Z_{real} and an imaginary part Z_{img} . This complex expression is usually best represented by a Nyquist plot ($-Z_{img}$ vs. Z_{real}) where the impedance is measured over a wide range of frequencies.

EIS is a powerful tool to explore and characterize membranes. It is currently used to many characterize a number of properties: dielectric [62], [63], resistance of ion-exchange membranes [64] and fouling [65], [66]. The EIS technique can provide a quantitative measurement of the bulk electrical resistance of the bulk electrolyte as well as the interfacial regions of membranes.

In the application of fuel cell gas sensing, the PEM is a major factor contributing to the ionic resistance of the MEA [18]. Since this work focuses only on the membrane and the sensor prototypes, the effect of fuel cell sensor and MEA will not be tested. The same GDE, the same MEA fabrication process and the same prototype system will be implemented throughout this study. Thus, to make characterization simpler, the synthesized membrane will be directly tested.

3.1.1.3.1.1. Through-plane conductivity

PBI membrane with different thicknesses, doped at different concentrations and at various temperatures will be characterized. To carry out these tests, a 3D design is made from a specialized polyetheretherketone (PEEK) plastic (TECAPEEK CMF white, Ensinger) with ceramic fillers that can sustain high temperatures, is resistive to acid and is electrically nonconductive. The design is confined at a constant pressure throughout the evaluations to ensure good contact was made.

For the setup, a 6 mm x 6 mm portion of the doped membrane is cut. This membrane sample is placed between two Pt foils that have a 5 mm x 5 mm overlapped area shown in Figure 3-3. This overlapping area was used to evaluate the proton conductivity. A 10lb force is applied to each assembly with a torque wrench (FAT Wrench 5553556) and placed inside a heated glass vessel controlled by a PID controller. The goal of this setup is to replicate environment within the fuel cell sensor prototype.

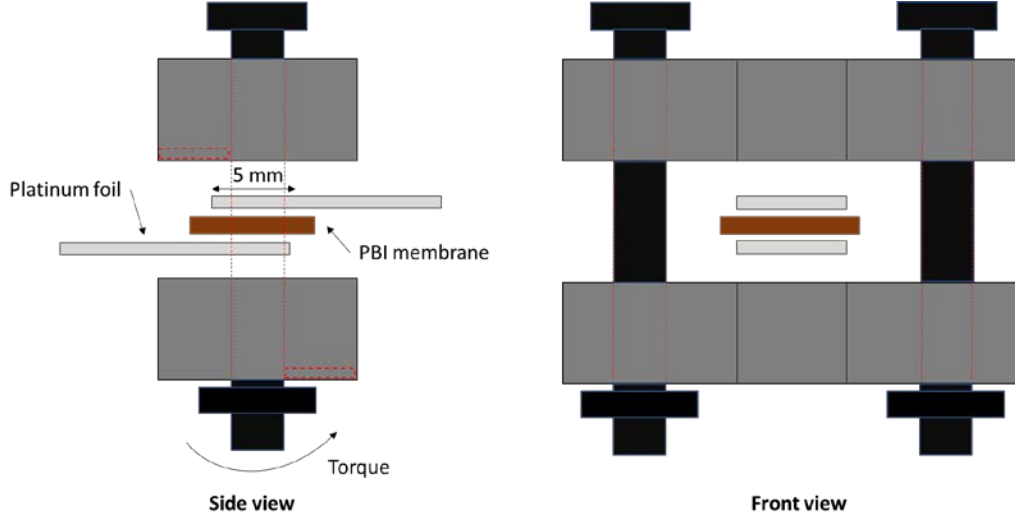


Figure 3-3: Through-plane 3D Design and Pt foil and Membrane Layout

The EIS test is carried out using a Princeton VersaSTAT MC potentiostat. The testing parameters are 0.0 V bias vs. OC DC and 300 mV RMS AC scanned from 1MHz to 100Hz. The signal sampling was set to collect 30 points per decade. To determine the membrane ionic resistance, the high frequency responses are linearly extrapolated to the Z_{real} axis. This x-intercept value is interpreted as the ionic resistance of the membrane.

The conductivity of the membrane was calculated by the following equation:

$$\sigma = \frac{l}{R A} \quad (4)$$

where,

σ = membrane conductivity

l = thickness of the membrane

R = membrane ionic resistance

A = cross sectional area of the tested membrane sample

3.1.1.3.2. Scanning Electron Microscopy (SEM)

Scanning electron microscopy (SEM) is a technique which uses a focused beam of electrons to produce images of a surface of sample. This is done by detecting and analyzing the interaction between the surface atoms and the electrons. Different surface topographies and compositions will produce different interactions. The most common detection mode for SEM involved the detection of the secondary electrons. These secondary electrons are emitted by the sample atoms excited by the electron beam. Using a spatial detector that can detect these secondary electrons, an image of the topography of the surface can be formed [67]. In this work, a SEM was used to examine the morphology of the sPBI and pPBI membrane. The SEM was performed with a LEO 1530 FESEM to obtain the SEM images.

3.1.2. Gas Diffusion Electrode

The GDE is purchased from FuelCellEtc and used without any further modifications. The GDE is contacted with built on a non-woven carbon paper with a MPL that contains 5%wt PTFE as binder and with a total thickness of 235 μ m. The CL layer contains 60% Pt on Vulcan Carbon support. The Pt loading is 0.5mg/cm². The GDE also has a thin layer of Nafion[®] coated on top as a final step to improve the adhesion with the membrane. A full description of the GDE fabrication process can be found elsewhere [68].

3.1.3. Membrane Electrode Assembly Fabrication

The MEA is fabricated by punching a doped PBI membrane into a circular shape with a diameter of 18 mm. Two GDE are also punched into a circular shape but with a smaller diameter of 16mm. The two GDEs sandwich the PBI membrane. The GDEs are aligned to overlap on top of each other while staying completely within the larger PBI membrane area. Such an arrangement aims to account for the possible sliding of GDE on top of the membrane during testing as well as preventing any localized short circuits at the edge of the MEA. The hot press condition is set to 250 PSI at 130°C for 180 seconds. Figure 3-4 depicts the arrangement of the MEA.

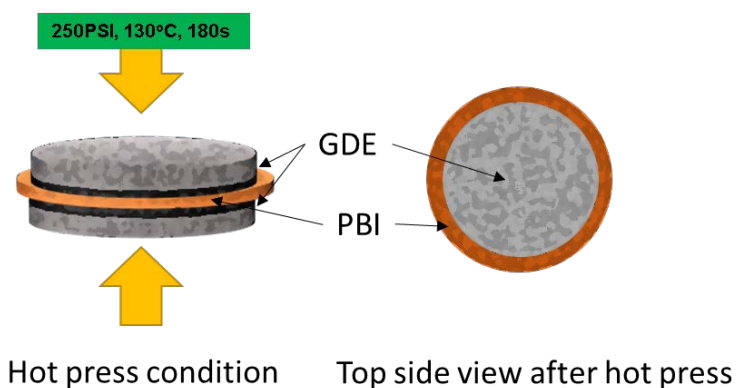


Figure 3-4: MEA Hot Press Condition and GDE Alignment

After hot pressing, the MEA is left to cool down at ambient conditions and stored inside a H_3PO_4 chamber. The MEAs are positioned vertically in a stainless-steel spring and then placed inside a chamber containing a small amount of H_3PO_4 . The MEAs are partially submerged into the acid. The chamber is completely air tight once sealed. When the MEAs are not being test, they are stored in this chamber. Figure 3-5 depicts the storing process. The MEAs remain in the chamber for at least 24 hours after hot-pressing to re-equilibrate with the acid before it is tested in a fuel cell.

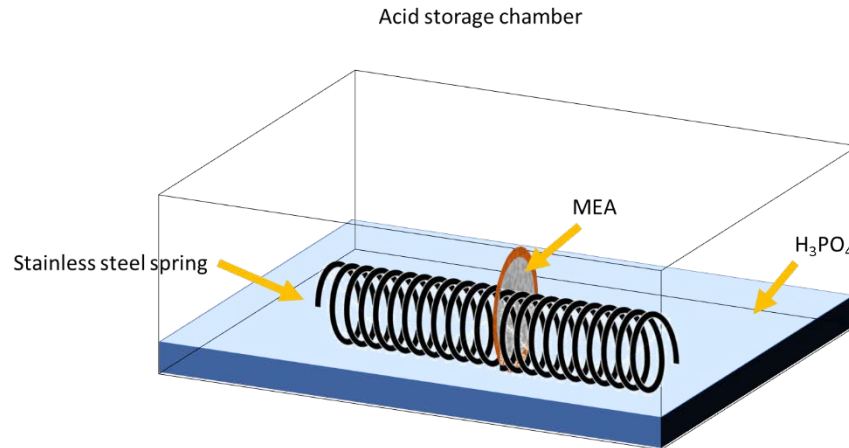


Figure 3-5: Phosphoric Acid Storage Chamber for MEAs

3.2. System Design

3.2.1. Sensor Housing Design

3.2.1.1. Design Requirements

Considering the size of the MEA and conditions at which it is to be tested under (e.g. concentrated acid, high temperature, etc.), the sensor housing must satisfy the following requirements:

- Material requirements
 1. Acid resistant
 2. High temperature resistant (at least up to 200°C for a prolonged period)
 3. Easily machinable
 4. Electrically insulating
- Required features
 1. Enable multiple uses, quick test setup
 2. Easy connection to external logging devices, pumps, etc.
 3. Able to accommodate various MEA dimensions
 4. Provide reliable and repeatable measurement across different MEAs
 5. Easy heating and temperature distribution and control

6. Good distribution of analyte gas sample on the anode
7. Minimal leakage or crossover between cathode and anode, as well as the housing from the outside environment
8. No external insulation due to other elements incorporated to the housing

Many materials are available for the sensor housing. The two most accessible types are plastic or ceramic materials. In general, plastic materials are more economical and easier to machine especially at the micrometer to centimeter scale. Additionally, local workshops are better equipped to handle plastic materials. Thus, plastic is the better choice for the housing.

In terms of design features, with the exception of requirement #5, every requirement is a passive feature that can be addressed through iterative designs of the internal of the housing. Criteria #5 is the only active component of this housing and is an essential part to the testing. To address #5, the housing can be designed to accommodate a heating element on its interior or exterior. If an interior heating element is to be used, the heating element will be in direct contact with the MEA and enclosed within the housing. In the case of an exterior heater, the element will partially cover the housing. Each of these design choices has advantages and disadvantages, as summarized in Table 3-1 :

Table 3-1: Comparison Between the Inside and Outside Position for Heating Element

	Advantages	Disadvantages
Inside	<ul style="list-style-type: none"> - Faster heating - Direct MEA temperature monitoring - Quicker response for temperature control 	<ul style="list-style-type: none"> - Heat gradient generated with different MEA thicknesses - Quicker degradation of MEA due to direct heat exposure - The MEA is perturbed during operation
Outside	<ul style="list-style-type: none"> - Minimal perturbation to MEA during operation - More internal design space to accommodate other features - Smaller MEA temperature fluctuation 	<ul style="list-style-type: none"> - Requires more power and finer temperature control - MEA perturbed during operation (if probe is placed inside) - Slower heating

To properly select a suitable design for the housing, two 3D designs have been built. Each design is comprised of two parts: MEA container (bottom) and the seal (top). Both MEA containers

have the same internal design but the sealing is different. One seal is designed to allow the heater to be attached on the outside while the other for the inside. The following section describes these two designs.

3.2.1.2. MEA containers

Figure 3-6 left shows the baffled path through which the gas analyte travels on the anode side during operation. This design creates a turbulent flow and distributes the analyte evenly across the anode side of the MEA. The baffle thickness is also designed to properly support the MEA without covering the MEA surface. The pattern takes up approximately 27% of the total area of the MEA. The locations where the gas analyte enters and exits are indicated in Figure 3-6.

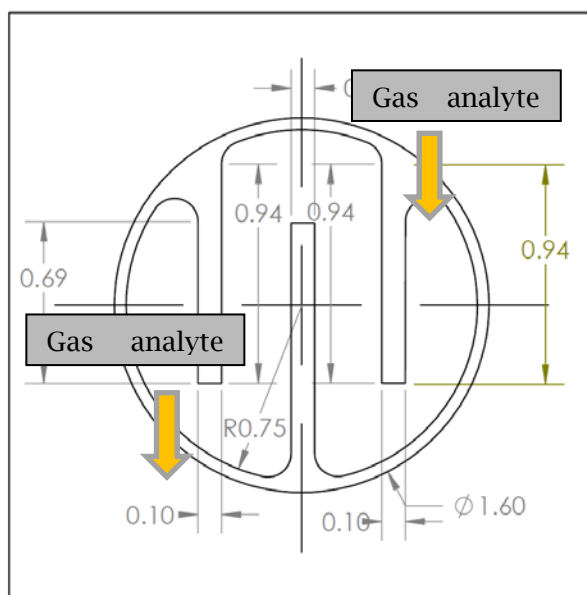


Figure 3-6: MEA Containers Design. Left: gas analyte travel part; dimensions are in cm

3.2.1.2.1. Heating Element Inside (HEI) Design

To implement a heating element on the inside, SolidWorks 2015, a computer aid design (CAD) program, is used to render the base pattern in Figure 3-6 into an appropriate 3D structure. This structure is made from PTFE, which has good thermal insulation properties and excellent chemical resistance. Its operating temperature range is also suitable for the application since its

melting point well over 420°C. Figure 3-7 shows the final 3D rendered design. The MEA container dimensions are measured at 2.5 cm x 2.5 cm x 1 cm.

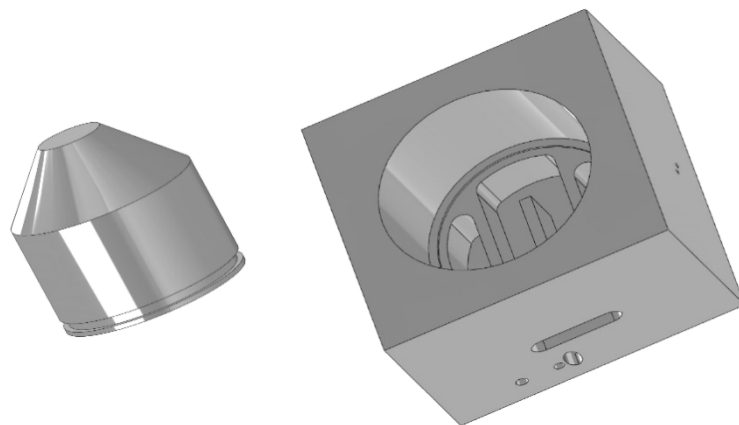


Figure 3-7: 3D-rendered Heat Element for Inside Implementation

Left: 3D Rendering of the Seal; Right: 3D Rendering of the MEA Container

For the assembly of the fuel cell, the MEA is placed at the bottom of the container on top of the baffle pattern. The seal is thereafter inserted into the container to contact the MEA. The seal has a groove at the bottom end to accommodate an O-ring for further sealing during operation. The MEA container has several slits for inserting Pt wires, heating element, temperature probe and stainless-steel tubing. A pair of Pt wires act as connectors from the cathode and anode to the current/potentiometer. The heating element and the temperature probe are located on top of the MEA (the cathode side).

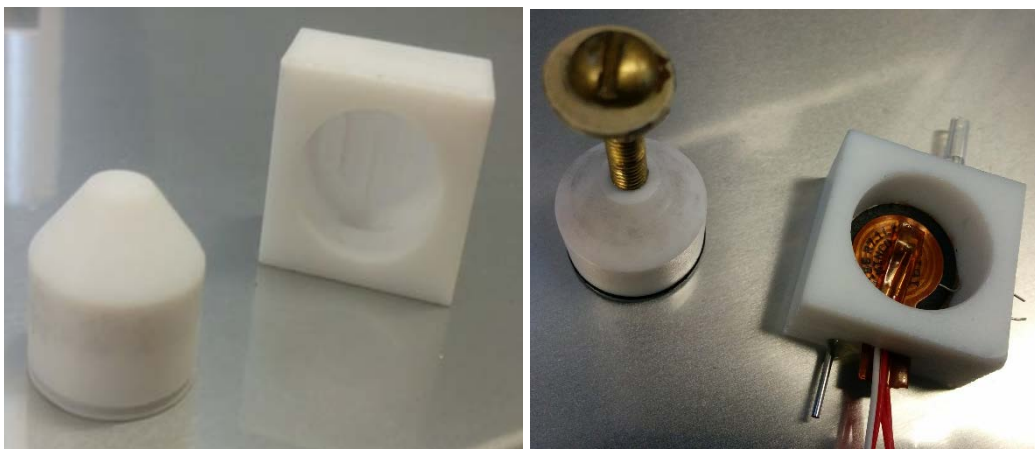


Figure 3-8: Left: As made PTFE Housing; Right: Set-up before Operation

The heating element is a Mod-Tronic Kapton heater with silicone rubber insulation (HK5186R7.1L12F, MINCO). The heating element has a donut shape with 0.5" OD and 0.09" ID with. The heating element resistance is 7 ohms and can operate up to 204°C. The temperature probe is an RTD sensor made of Pt and rated at 100 ohms. Figure 3-8 shows an as-made PTFE housing and the assembly of all the elements prior to testing. The overall dimension of the MEA container is 2.5 cm x 2.5 cm x 0.5 cm.

3.2.1.2.2. Heating Element Outside (HEO) Design

To implement the heater on the outside, a few alterations are made. Firstly, the material must be able to conduct heat very quickly and efficiently. Thus, instead of using PTFE to trap the heat within the housing, PEEK (TECAPEEK CMF white, Ensinger) material used for EIS test is the ideal candidate as it has all the requirements. The MEA container design is essentially the same as before except the height is significantly lower because the heat emanates from outside the housing and the rate of heat transfer is increased by minimizing the thickness of the housing wall. It is also worth noting that the volume of the space that contain the baffle pattern is identical in both heating element implementations on the anode side. This enables more controlled comparison between the two housing designs. Figure 3-9 shows the 3D render of the designs. The seal has a flat side to allow intimate contact with the heating element. The seal also contains an O-ring to provide air seal.

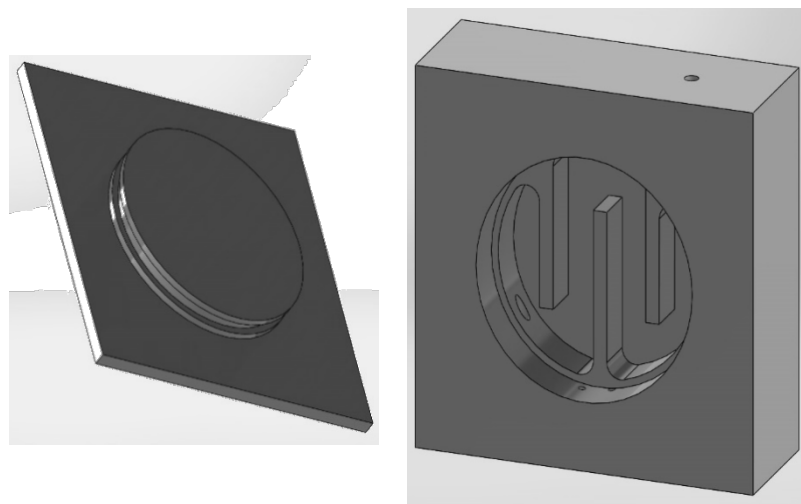


Figure 3-9: 3D-rendered Heat Element Outside Implementation

Left: 3D Rendering of the Seal; Right: 3D Rendering of the MEA Container

This design used two 1" x 1" heating elements (HR5163R5.6L12B, Minco) provided by Mod-tronic. Each element adheres onto two square sides of the housing. A single Pt probe was used on the outside. To ensure the accuracy of the MEA temperature, the heating elements are

firstly calibrated by inserting the probe inside without any MEA. The heating element is a Kapton heater with rubber insulator. Figure 3-10 shows the as-made housing and the set up.

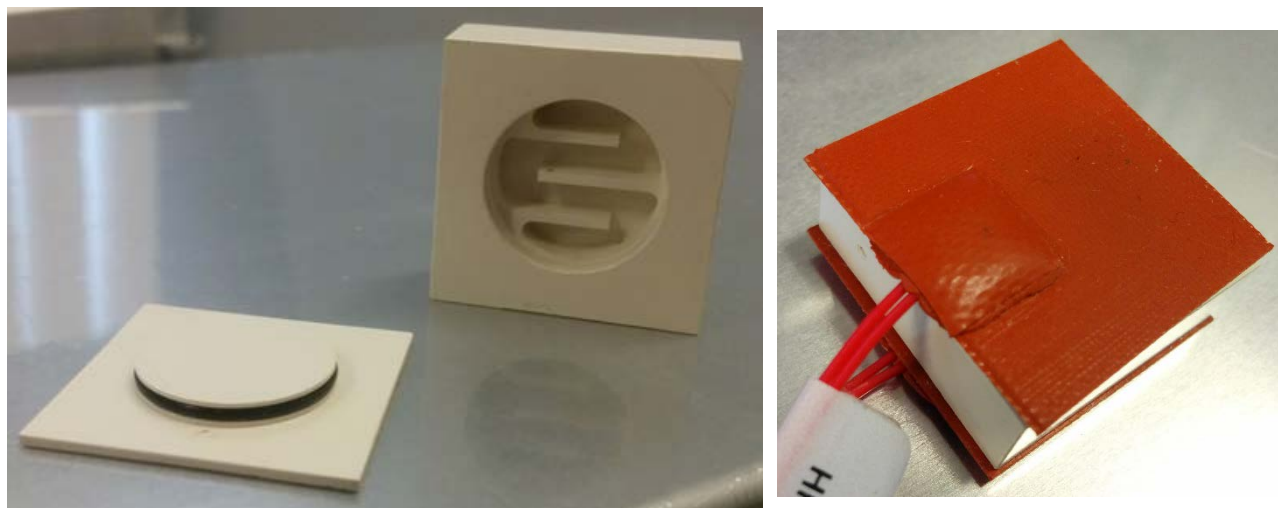


Figure 3-10: Left: As made PEEK Housing; Right: Set up before testing

The MEA is positioned in such a way that its distance between the two heat elements are equal. This ensures that there is a negligible temperature gradient on both sides of the MEA during operation. Both housing designs contains the same volume of 0.5mL for the gas analyte on the anode side.

3.3. Fuel Cell Sensor Testing

3.3.1. Fuel Cell Test Set-up

Three components make up the fuel cell test apparatus: temperature controller, gas sampling controller and data acquisition device. The follow subsections describes each of these components in detail.

3.3.1.1. Temperature Control

A DC PID controller (CT325PD2C1, Minco) purchased from Mod-Tronic was initially considered and tested. This PID controller can both monitor and control the heating element temperature. However, the control action of the controller affects the sensor signal significantly.

The signals from the sensor are usually in the range of μV to mV . The actions of the controller create a sinusoidal fluctuation in the μV range. The frequency of this fluctuation is directly related to the initial applied voltage; the lower the voltage, the frequency. Fortunately, this effect can be mitigated by lower the controlling voltage. However, this will in turn slow down the heating rate and magnify the temperature oscillations about the set point. Overall, lower the controlling temperature defeats the purpose of having a PID controller.

To circumvent these problems with the PID, temperature control is achieved by using a LM2596 DC-DC 3A adjustable buck regulator power module with 4-digit potential meter precision (CST2013001). The 4-digit potential indicator allows fine control of the constant voltage input into the heater and proper calibration of the voltage and temperature. Once the calibration is completed, the heating element can be raised very quickly to the desired temperature and the voltage quickly set back down to the corresponding calibrated voltage. While this method is slower than using a PID, the constant voltage applied produced negligible signal interference once stabilized. To summarize, the PID can control and reach the heating element desired temperature within 1 or 2 minutes, while the LM2596 can raise the temperature and stabilize with 5 to 10 minutes. Another advantage of its use lack elimination of a temperature shock to the MEA, i.e. the large gradient created by the rapid heating from the PID controller throughout operation can potentially damage the MEA. The slower temperature increase by LM2596 is more favourable for the MEA stability. While the PID controller is not used to control the heating element temperature, the temperature monitor function is utilized in conjunction with the LM2596.

3.3.1.2. Sampling Control

3.3.1.2.1. Acetone Gas Sample

To collect the necessary gas samples and assess the sensor prototypes, a 500mL (GUTH Model 12V500) breath simulator is used. This simulator can reliably generate many thousands of gas samples while maintaining a high level of accuracy. The simulator generates a gas analyte sample by bubbling air through a dilute solution of acetone or any analyte of interest. The

solution is maintained at 34°C to simulate a gas sample that closely resembles human breath. The advantages of using this breath generator are: (1) its small and compact size and portability compared to that of a compressed gas cylinder, (2) quick, easy and inexpensive setup for testing, (3) applicable to any analyte of interest, (4) ability to gather relevant data related to healthcare applications such as blood glucose monitor and diagnosis for diabetes.

Starting with a 500mL acetone-DI water solution (4% vol. acetone) as stock, various volumes of this stock solution can be added to a 500mL DI water to vary the concentrations of the acetone solutions. To determine the concentration of the gas analyte in the vapour phase for a known diluted solution, Henry's law is applied. The acetone and water binary systems have been well studied and documented [69], [70]. The detailed calculation procedure for the analyte concentration is given in the Appendix.

3.3.1.2.2. Gas Sampling

To maintain sensor accuracy and minimize the variability during testing, an automated sampling system is designed to accommodate the breath simulator. An air pump and sampling pump are used to deliver the air to the simulator and the analyte saturated gas from the simulator to the sensor respectively. A 2-relay module (Numato Lab) that can be connected and controlled by a PC is selected to do achieve this. The relay contains a microcontroller that can be programmed to precisely control pumps in any configuration. Figure 3-12 illustrates how the relays are wired to the pumps.

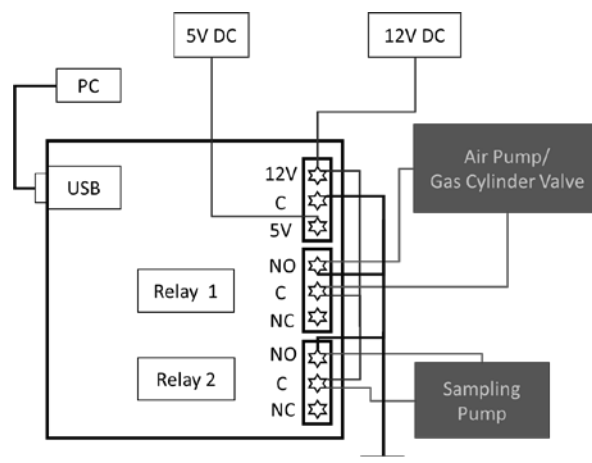


Figure 3-12: Two-relay Module Wiring and Set-up

The air pump used is a specialized 12V DC pump (BOXER PUMPS LONDON 3112.121/12V) that can deliver up to 18L/min gas. More specifically, a solenoid pump (AAA120128, Alcohol Countermeasure System) is used. The solenoid pump operates by first running a current through a metallic coil, magnetizing it, which in turn pulls a piston and brings air into the chamber. By supplying a fixed amount of current each cycle, this mechanism allows the solenoid pump to consistently extract a fixed amount of gas analyte. This is ideal for testing different MEAs under similar conditions. This pump has a capacity of 2mL, which is much larger than the volume of the housing anode side. This ensures that the gas analyte completely displaces the dead volume inside the housing during testing and thereby provide reliable and repeatable testing conditions.

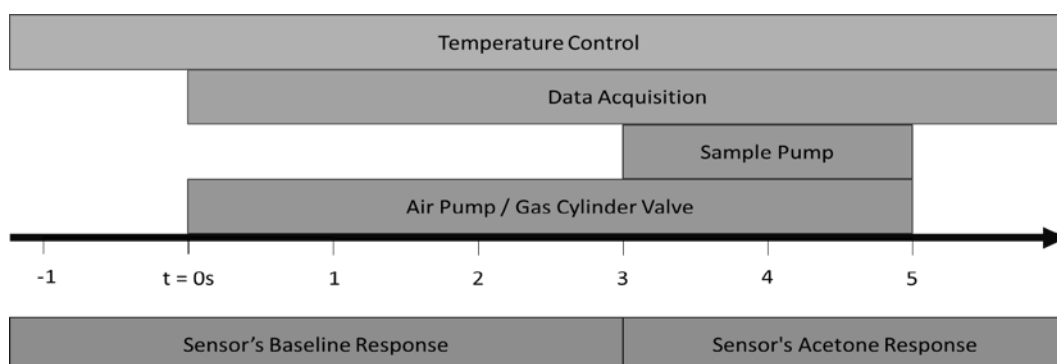


Figure 3-11: One Sensor Test Cycle Operation Timing of Different Components

By controlling the relays through the computer, the two pumps (or gas cylinder valve) can be set to run at set intervals. At the start of each test cycle, the air pump/gas cylinder valve is triggered at the same time the data acquisition system begins to log the sensor output. This step lasts for 5 seconds. After 3 seconds, the sampling pump is activated, and the gas analyte is pulled through the housing. Figure 3-11 shows the operating structure and timing for each component.

3.3.1.2.3. Data acquisition

The data acquisition component is completely automated. The sensor signals are monitored by a digital multimeter (DMM) (34411A, 6^{1/2} digit, Keysight Technologies (formerly Agilent Electronic Measurement)). Typically, the fuel cell sensor signal in this study goes as low as single digit microampere. The DMM can detect signals as low as 100 picoamperes and provide a 10³ signal-to-noise ratio. The signal can be logged with software that accompanies the DMM, i.e. Keysight Benchvue. Using this software, the user can select the type of signals the DMM is measuring, as well as the starting point of the measurements. The software also allows the logged data to be generated in either a MatLAB or a comma-separated value (CSV) format. The software has an application that enables automatic DMM trigger, data logging and data exporting called Benchvue WorkFlow. This application allows the user to specify routine for the DMM as well as how the software will treat the logged data afterward. The application also allows user to run a

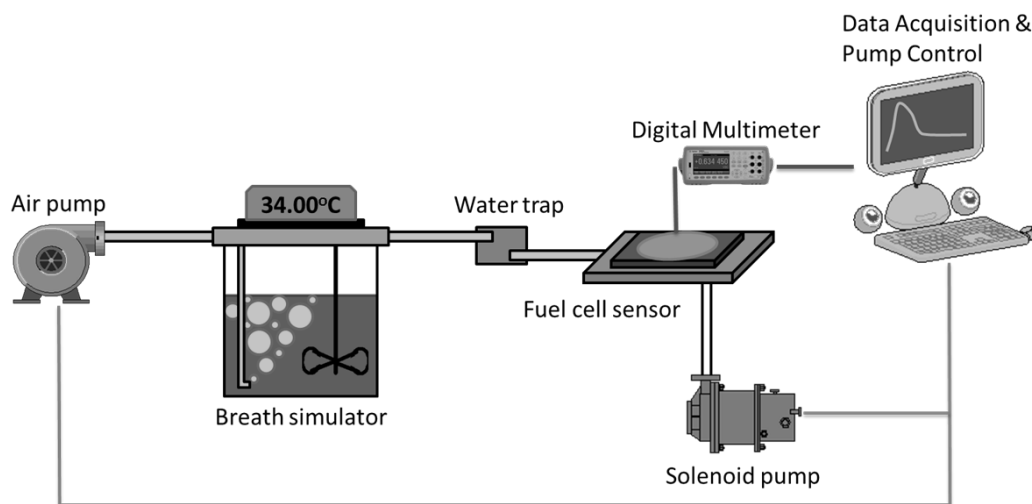


Figure 3-13: Schematic Overview of the Fuel Cell Test Set-up

programming script to control external programs and/or devices to control the external gas sampling component. A Python script to coordinates the pumps with the Benchvue WorkFlow routine to ensure reliable and consistent test cycles. Within the Benchvue WorkFlow routine, the user can specify the number of cycles and duration of each cycle for each test. The user can modify the trigger timing as well as the ON/OFF duration of each pump separately. These features give the user complete and intuitive control on the fuel cell test routine as well as the ability to alter the hardware operation. This allows the user to modify the setup in the future to adapt to any possible changes required. Figure 3-13 is a schematic of the fuel cell test set up. Figure 3-14 is a photograph of the fuel cell test set-up during operation.

The fuel cell sensor cathode and anode Pt lead are connected in parallel to a 20-ohm resistor and then the DMM leads are connected to the two terminals of the resistor. The DMM measures the DC voltage across the resistor. Afterwards, this data is taken as the sensor response. The addition of the resistor to the sensing circuit removes the noise from the fuel cell. This also allows more flexibility converting from current to potential during the data analysis process.

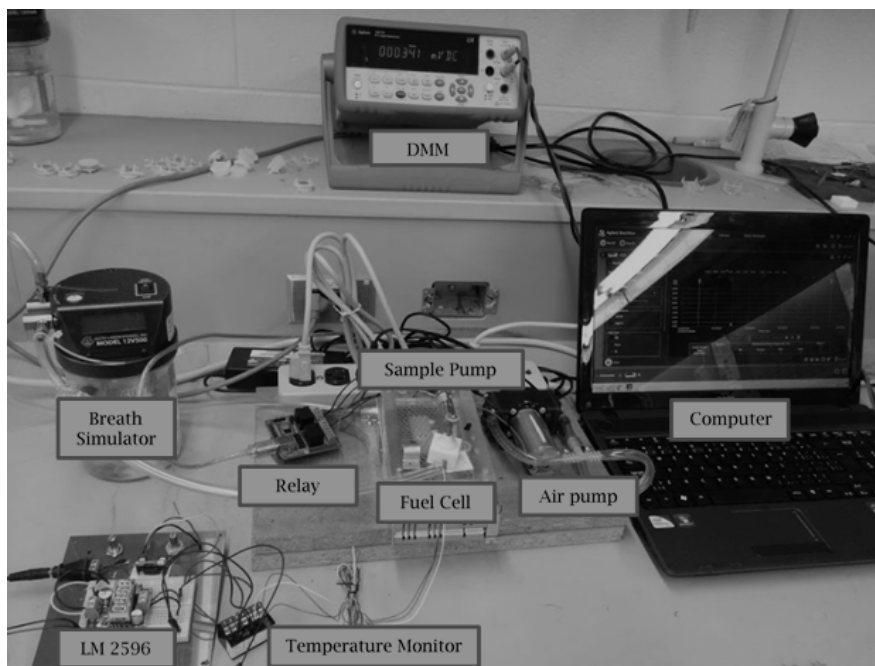


Figure 3-14: Fuel Cell Test-up During Operation

3.3.2. Sensor Response Curve and Data Analysis

The final step of the fuel cell test process is the data analysis. The data are converted to current to be more in-line with industry and literature procedure. To analyze the sensor response curve, a widely used method from the breath alcohol fuel cell industry is implemented [18]. Figure 3-15 demonstrates this approach. After reaching the peak, the sensors response starts to relax back to toward the baseline or the initial zero point. In most instances, this relaxation follows an exponential decay equation. To shorten the calculation time and avoid baseline drift, certain points along the relaxation curve are used to approximate the total area of the response curve.

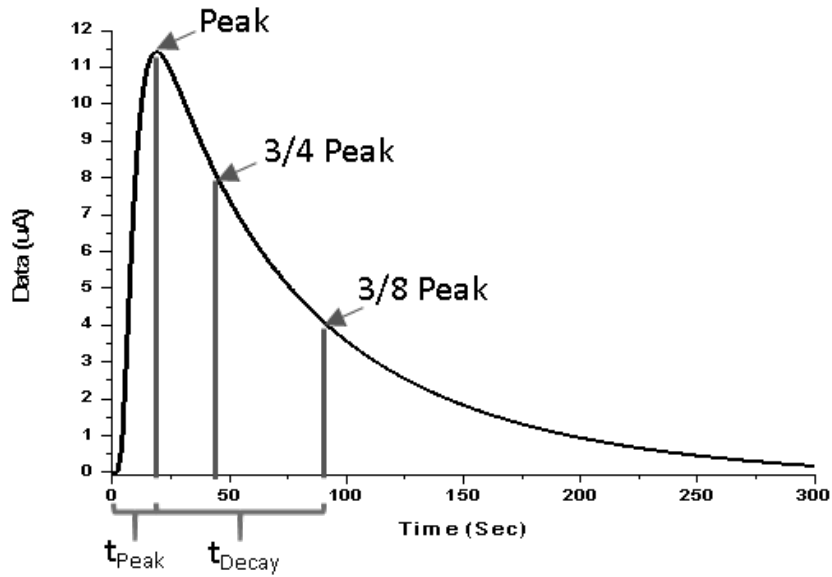


Figure 3-15: Typical Fuel Cell Sensor Response Curve and Key Characteristics

Figure 3-15 illustrates a typical response curve and the points used to estimate the total area under the curve. To make this estimation, the peak point is first identified. Then, the point 3/4 and 3/8 value of the peak are calculated. The total area can be estimated by the following equation:

$$Q_{total} = \int_0^{A_3/4} A \cdot dt + 2 \left(\int_0^{A_3/8} A \cdot dt - \int_0^{A_3/4} A \cdot dt \right) \quad (5)$$

This mathematical analysis is carried out using OriginPro 8.5, via the peak analysis function to identify the peak and other characteristics. Since the response curve is relatively smooth with a non-fixed interval, a one-third Simpson or a Gaussian quadrature method can be applied to estimate the area under the curve.

Furthermore, two more characteristics of the response curve can be drawn from Figure 3-15: time-to-peak and decay-time. In this test set-up, time-to-peak (t_{peak}) is defined as the time, in seconds, between the triggering of the sample pump (Figure 3-10) and the peak response value. The decay-time is defined as the time required for the sensor's signal to relax from the peak to the $3/8^{\text{th}}$ peak value. Typical fuel cell sensors have a combined time-to-peak and decay-time of less than 30 seconds. These two values are the primary indicators in gauging commercial fuel cell sensors.

3.3.2.1. Response Curve Area and Analyte Concentration

The area under the response curve is directly correlated with the analyte concentration. Faraday's laws of electrolysis (eq. 6) can be used to explain this relationship. Specifically, in each anodic (acetone oxidation) reaction, the amount of species that reacts is related to the current applied or generated over a certain period. This relationship is mathematically expressed as followed:

$$n = \left(\frac{Q}{F}\right) \left(\frac{1}{z}\right) \quad (6)$$

Where,

n = the amount of substance in moles

Q = total electrical charge passed through the substance in coulombs

F = Faraday's constant, 96500 C mol^{-1}

z = electrons transferred per ions

When the current is time dependent, Q is calculated by integrating the current over time i.e.,

$$Q = \int_0^t I(\tau) d\tau \quad (7)$$

In this work, the area under the response curve represents the amount of electronic charge passing through the circuit. With the amount of gas analyte fixed (i.e. at 2mL per sampling cycle), the area under curve should ideally vary linearly with the concentration of the analyte. This is valid under the assumption that the background noise and interferences within the system remains at similar levels and only changes in the analyte concentration contribute to the variation of the response curves and consequently, the curve area. This theoretical assumption relies on two important factors: (1) calibration, (2) determination of detection limit. Using the linear relationship, one can calibrate the sensor by correlating the signal responses to known analyte concentrations. Consequently, this calibration can then be used to calculate unknown concentrations of analyte. Repeated calibrations can be used to estimate the error, which can be used to determine the minimum detectable concentration of an analyte. The errors will provide statistically-sound guidelines on whether to treat a signal as noise, or as a real response when dealing with very low concentration of analyte. The higher the area, the higher are its sensitivity and detection limit.

3.3.3. Experiment Outline

The experimental plan has 3 main steps, listed in order of execution below:

1. Determination of the best heating element implementation and design for fuel cell sensor testing
2. Characterization of the acid-doped membrane in terms of thickness, temperature, doping acid concentration and porosity
3. MEA fabrication and fuel cell sensor performance optimization based on the membrane characterization results

4. Results and Discussion

4.1. Sensor Housing Design

Both sensor housing designs were tested with their respective heating elements to determine the best option for further fuel cell sensor tests. The heating rate within the housing must be moderately fast but not too quick since large temperature gradients could damage the structure of the MEA due to excessive thermal stress. Thus, the operating temperatures were maintained in the range of 100 – 200°C and left the system to completely automate after the initial set-up. Thus, two for selecting the best design were based on how well the housing temperature can be controlled and how safe the device was during extended unsupervised operation.

Using the LM2596 generator, the HEI design took under 10 minutes to reach and stabilize at the desired temperature. The voltages of 3.5, 4.5 and 5.5 V correspond to heating element temperatures of 120, 140 and 180°C, respectively. At an MEA temperature of 180°C, the housing outside surface temperature and less than 100°C. This temperature was well below the heating limits of the other components. The housing could also be quickly detached from the setup to lower the hazard should electrical failures occur.

On another note, the HEO performed very poorly. It took more than 20 minutes for the housing to reach 140°C. Furthermore, when the inside temperature reached 140°C, the actual temperature of the heating element on the outside matched the limit of the heating element of 200°C. The LM2596 constant voltage was set to 6 V to account for the heat loss due to the four exposed sides of the housing. However, the heat loss rate due to these exposed sides was much more substantial. The advantage of the high thermal conductivity of the PEEK was not utilized much when very little of additional thermal insulation to prevent heat leakage. With the HEO design, temperatures greater than 140°C could not be reached since 204°C was the maximum rated temperature for the heater. Moreover, two heating elements was implemented in the HEO

design compared to one in the HEI design. These results show that the HEO is far less efficient than the HEI, notwithstanding the cost associated with setting up additional test setups. Overall the HEI design was a superior option and so in all further fuel cell sensor tests within this project.

4.2. Membrane Synthesis and Characterization

4.2.1. Membrane Synthesis

The initial trials of casting the sPBI were very difficult without using an aluminum foil covering the casting plate. The casted membranes were not homogenous and exhibited an uneven distribution of PBI, as shown in Figure 4-1. This occurred for most starting PBI weights. This discrepancy in the PBI distribution happened mainly due to the differences in the evaporative flux in the regions close to the center and to that at the edge of the stainless-steel wall. For regions closer to the wall, the flux was higher than the center due to the higher heat conductivity of the aluminum side wall, as opposed to air. This flux gradient caused the DMAC to push the PBI toward the center where the flux was slower. On the other hand, no problem with casting of the pPBI membranes were observed.



Figure 4-1: sPBI Membranes with Uneven PBI Distribution

To troubleshoot the casting process and prevent the unevenness of PBI distribution in the membrane, a few approaches were tried. Firstly, the viscosity of the solution could be tuned by varying the PBI concentration, i.e. a series of PBI-DMAC solutions at different PBI concentration from 5 – 15% w/w were cast at 90°C. Literature suggests that the viscosity will have a significant effect on the casting process, as well as the physical properties of the membrane post-casting [61], [71]–[74]. However, the solution viscosity increased as DMAC evaporated which made it difficult to control the viscosity and improve the final membrane. Another approach to control the evaporation rate was to control the casting temperature. Literature suggested a slow ramp and holding the temperature between 80 – 120°C [73], [74]. For this study, the membranes were cast at constant temperatures: 80°C, 90 °C and 100°C. At these three temperatures the uneven PBI distribution in the membrane persisted and in fact became worse with higher cast temperature. Speculatively, this was due higher temperature gradient between the edge and the center of the casting plate. It was clear that the evaporative flux gradient must be eliminated rather than manipulated. Although the casting process was carried out in a closed environment within an oven, the flux gradient needed to be controlled at the surface of the solution. To do this, aluminum foil was used to cover the casting plate during the process. This simple solution resolved the casting problem and the resulting sPBI membranes were very homogeneous upon visual inspection. Higher PBI concentrations (i.e. 10-12% w/w) and temperatures were investigated to optimize the process. The higher PBI concentration and cast temperature sped up the casting process. This method was also applied to cast pPBI with similar success to maintain the

consistency between two membrane morphologies. The final optimized procedure to synthesize sPBI and pPBI membranes is described in Chapter 3.1.1.



Figure 4-2: As-Made sPBI (left) and pPBI (right) Membranes After Recovery

After the membrane casting procedure was optimized, different thicknesses of sPBI and pPBI membranes were prepared. Figure 4-3 shows the variation of the average membrane thickness with the starting PBI weight and the resulting membrane thickness. Both types of membrane exhibited a linear relationship between membrane thickness and its PBI resin weight. Samples of the sPBI and pPBI membrane are showed in Figure 4-2. sPBI membranes were semitransparent while pPBI membranes were opaque with a lighter orange hue. The opacity is caused by the porosity introduced into the membrane by the DBP. Qualitatively, the sPBI membranes were stiffer than their pPBI counterpart, which implies that the stiffness of the sPBI increased substantially with increased thickness. However, the stiffness of pPBI membranes did not increase to the same degree. Only membranes with a thickness variation of less than $\pm 4\mu\text{m}$ were used for acid doping and MEA fabrication.

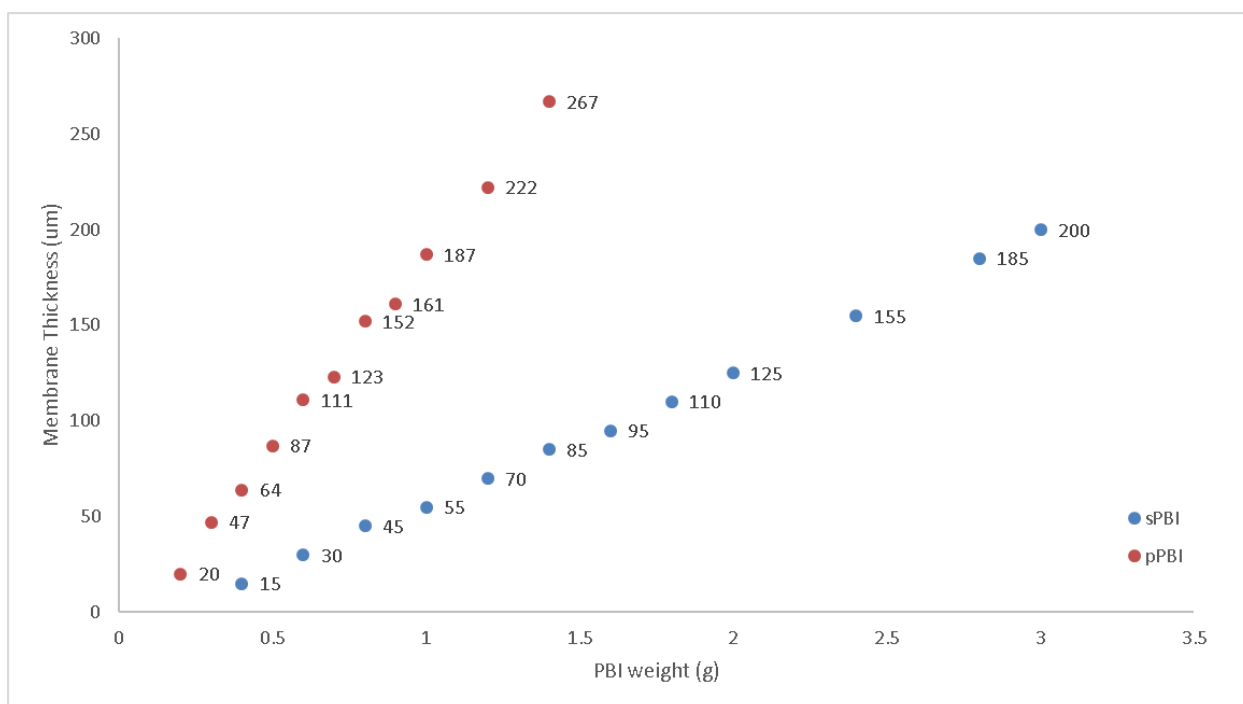


Figure 4-3: PBI Resin Weight vs. Thickness of the Membrane for sPBI and pPBI

4.2.2. Membrane Characterization

4.2.2.1. Through-plane Conductivity

4.2.2.1.1. Membrane Thickness

The through-plane conductivities of sPBI and pPBI membranes were tested as a function of their thickness. The test was conducted with an acid doping concentration of 5M H_3PO_4 and at 140°C. Each condition was replicated at least three times and the averages were calculated.

Figure 4-4 summarizes the through-plane conductivity test of sPBI and pPBI membranes over a thickness range of 20 – 200 μm . The anhydrous conductivity values of sPBI and pPBI membranes were in agreement with literature ranging between 25 - 200 mS/cm [75]–[81].

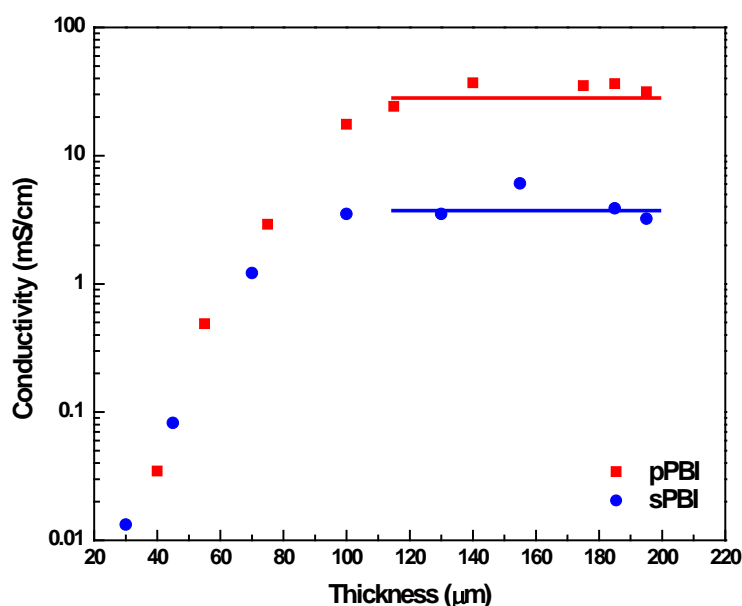


Figure 4-4: Effect of Thickness on Conductivities of sPBI and pPBI Membranes at an the Acid Doping Concentration of 5M H_3PO_4 and the temperature of 140°C

The through-plane conductivities of both sPBI and pPBI were very low at lower thicknesses sharply rose as the thickness increased. Notably, the conductivity of the pPBI membranes increased more than that of sPBI and overtook that of sPBI at a thickness of $\sim 80 \mu\text{m}$. In both cases, the conductivity leveled off when the thickness reached $\sim 100 \mu\text{m}$. At lower thicknesses, the concentrated acid can affect the structural integrity of the membrane [61][28]. Highly concentrated H_3PO_4 can actually dissolve PBI polymer when exposed for prolonged periods [81]. Inside the housing, higher temperatures and pressurized condition accelerated the degradation of the thinner membranes. As the thickness increased, the membranes mechanical integrity increased as well as their ability to resist thermal and compressive stresses. As a result, the conductivity of the membranes improved, even though the distance for the ion to the cross from one end to the other end also increases. This suggested that the porosity of had an indirect effect

on the conductivity. The increase in surface area as well as the amount of free acid contained within the porous matrix were likely the key contributors to this direct improvement. The increase in distance and the tortuosity of the pathway in which the ions must travel through from one end to another will inevitably decrease the membrane's effectiveness in conducting ions.

4.2.2.1.2. Acid Doping Concentration

Each membrane took a minimum of two weeks to prepare. Based on the results shown in Figure 4-14, we selected a membrane thickness of 100 μm for all subsequent experiments. The conductivity stopped increasing after the 100 μm . This suggested 100 μm is the minimal thickness for the best conductivity within the studied thickness range. Thicker membranes consumed more materials. Three levels of acid doping concentration were investigated: 2, 5 and 10M H_3PO_4 . Figure 4-5 showed a summary of the results.

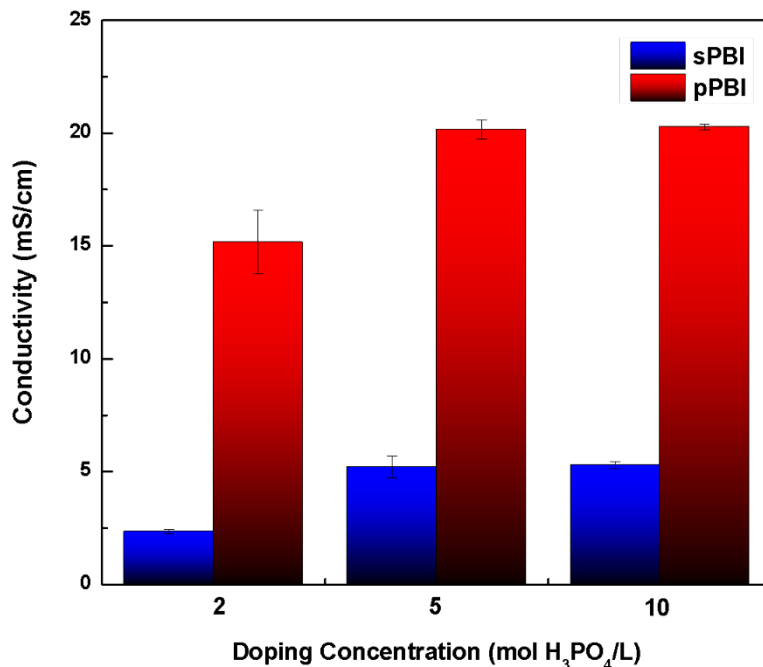


Figure 4-5: Through-plane Conductivities of sPBI and pPBI versus the Acid Doping Concentration; Membrane Thickness = 100um, Anhydrous, Temperature = 140°C

pPBI membranes exhibited higher through-plane conductivity than sPBI membrane at each concentration of acid doping. Interestingly, the conductivity of both pPBI and sPBI membranes stayed relatively constant at acid concentration of 5 and 10M. Results from previously mentioned literature were very clear on the effect of the acid doping concentration on membrane conductivity, i.e., the higher the acid doping concentration, the higher the ion conductivity that can be achieved at the cost of its mechanical strength and structural integrity. Numerous studies suggested a medium level of acid concentration to be used to dope the PBI membranes for optimal mechanical strength [82], [83]. While the elevated temperature and higher doping acid concentrations should have resulted in a higher conductivity, the combination of high temperature, anhydrous condition and higher acid concentration negatively affected the membrane mechanical properties. The similar conductivity values at 5 and 10M suggested that the negative factors outweighed the positive ones. The consistent trends shown by pPBI and sPBI

further supported the hypothesis that the introduction of pores was the cause of the improvement in conductivity.

4.2.2.1.3. Temperature

Literature has suggested operating temperatures from 100 to 180°C lead to the best performance and proton conductivity [28], [39], [72], [77], [82]-[85]. For this study, the in-plane conductivity was measured at three temperatures: 100, 140 and 180°C. Based on the previous experiments, the thickness and acid doping were set at 100 μ m and 5M, respectively. Figure 4-6 summarizes the conductivity of the pPBI and sPBI membranes at these three temperatures.

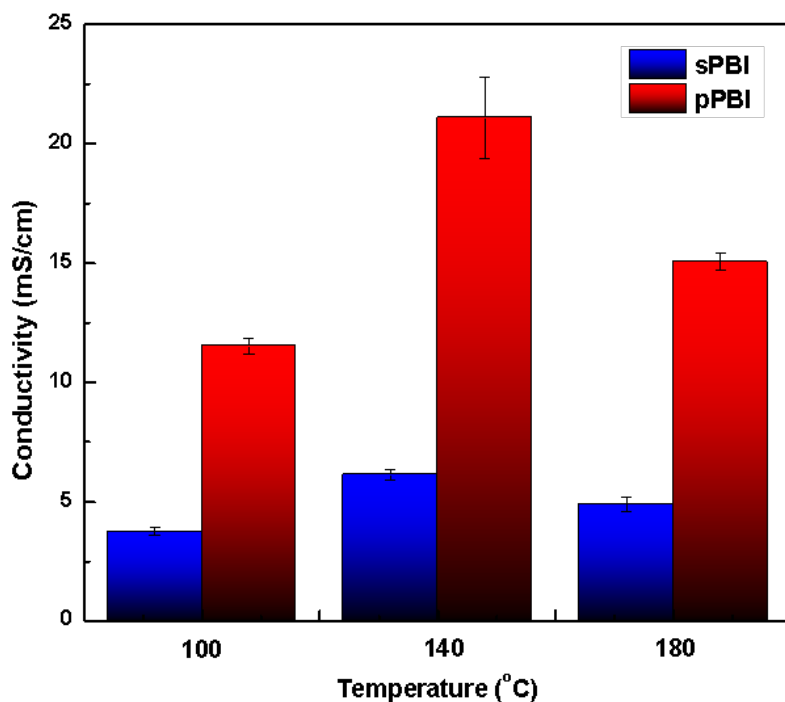


Figure 4-6: Through-plane Conductivities of sPBI and pPBI versus the Temperature; Membrane Thickness = 100 μ m, Anhydrous, Acid Doping Concentration = 5M

Similar to previous conductivity studies, the conductivity of pPBI was higher than that of sPBI membranes. For both morphologies, the conductivity increased from 100 to 140°C as

expected. However, with a further increase in temperature to 180°C the conductivity of the membranes decreased. For the pPBI membrane, the decrease in conductivity was substantial at 30%. This decrease in conductivity can be attributed to the anhydrous conditions and the high temperatures. These two factors can negatively affect the membrane structural integrity and mechanical strength. The compressive stress applied by the conductivity setup could further exacerbate this issue. This was not an ideal response since higher temperatures lead to faster reaction kinetics and less catalyst poisoning. It has been reported in the literature that higher molecular weight PBI polymers fared better at higher temperatures, but increasing the molecular weight and resulting viscosity pose problems for dissolution and membrane casting [29], [38], [61], [71], [74]–[78]. The PBI resin used in this work has an intrinsic viscosity (IV) of 0.5 which made it very easy to dissolve in DMAC but was lower than that reported in the literature [74]. Thus, this could be another factor affecting the membrane conductivity at higher temperature.

4.2.2.2. SEM Images

Figure 4-7 shows SEM images of the sPBI and pPBI membranes. These membranes were imaged prior to the acid doping. The sPBI membrane has an orderly, stacked-layer morphology of PBI crystals. The pPBI membrane image reveal a high porous structure with pores ranging from 5 to 15 μm in diameter. It contains a substantial amount of empty space where the acid can be contained. This enables a larger acid reservoir and therefore a more extensive proton conduction network. This could explain why the doped pPBI membrane tended to have higher conductivity than sPBI membrane.

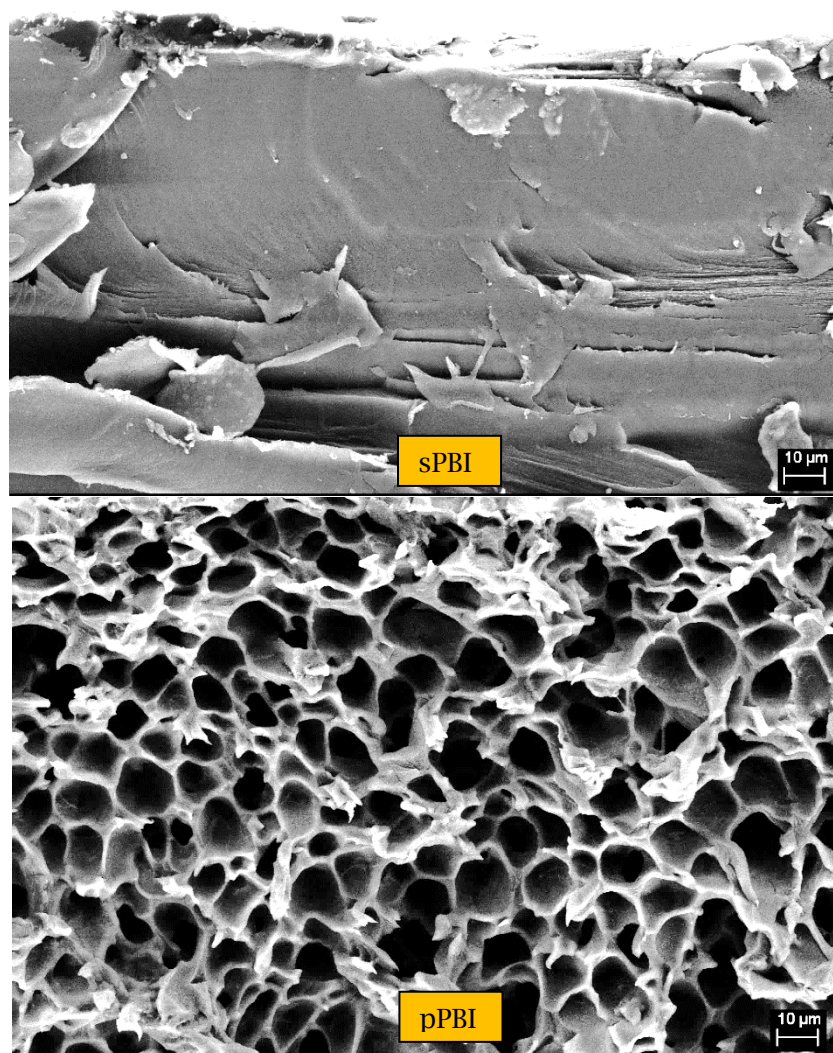


Figure 4-7: Cross-section SEM Images of sPBI and pPBI Membranes

4.3. MEA Fabrication

The MEAs were prepared after the 5-day acid doping process described in Chapter 3.1.1.2. Initially, the MEAs were made by stamping the GDEs and the membrane with the same diameter (i.e. 16 mm). The resulting MEAs were found to have a high rate of failure and highly variable sensing performance. Screening tests on hot-press parameters such as temperature, press duration and the pressure did not have a strong effect on MEA success. The arrangement and the topography of the MEA was investigated next. It was discovered that despite excellent alignment of the MEAs and membrane prior to hot-pressing, the application of pressure and temperature slightly displaced this alignment and often produced a localized short circuit at the edge of the MEA. Thus, a simple solution that proved to be successful was to stamp the MEA to a larger diameter of 18mm. This small alteration to the design eliminated the large variability between MEAs made from the same membrane and acid doping concentration. The optimized MEA fabrication process was described in detail in Chapter 3.1.3. Figure 4-8 shows a freshly made MEA next to a quarter for size reference.



Figure 4-8: As-Made MEA from a SPBI Membrane with a quarter for size comparison

4.4. Sensor Performance and Optimization

4.4.1. Thickness

MEAs made with different membrane thicknesses were tested in the sensor housing. The sensor housing, test procedure and response curve analyses were described in Chapter 3.3. These experiments were conducted at 140°C and an acid doping concentration of 5M H_3PO_4 . The thickness of the membranes was varied between 15 and 200 μm . The same membranes used in the conductivity studies were also used for the sensor performance test to ensure consistency and repeatability. The effect of thickness on the area under the response curve is shown in Figure 4-9. All the tests were conducted with 620 ppmv acetone.

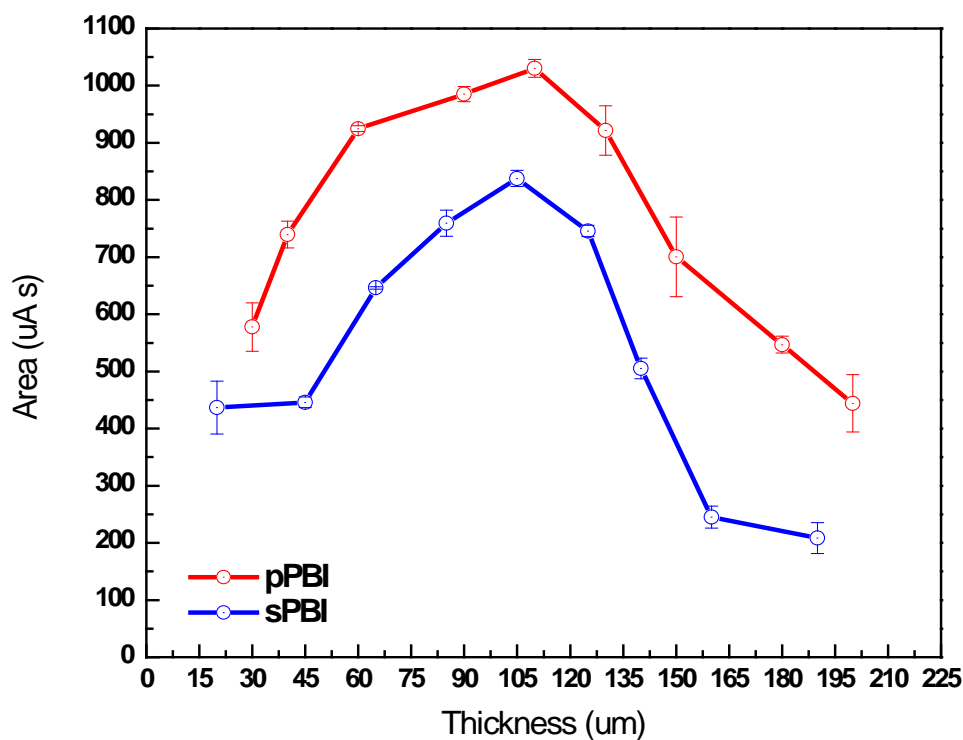
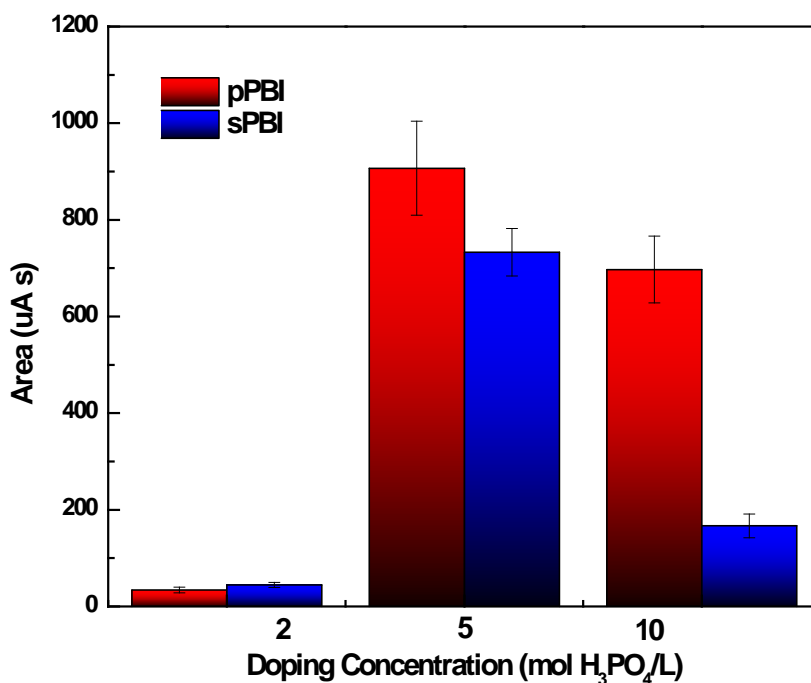


Figure 4-9: Fuel Cell Sensor Performance for 620ppm Acetone;
Acid Doping Concentration = 5M, Temperature = 140°C

Despite similar conductivities at lower thicknesses, the pPBI outperformed sPBI in the fuel cell sensor test at all thicknesses. This could be due to the higher amount of free acid contained within the porous matrix. With thinner membranes, the conductivity lowered, this may contribute to lower sensing performance. Fuel crossover rates are likely to be high and mechanical strength lower in thinner membranes. Additionally, the weaker mechanical strength at higher temperature and anhydrous condition combined with low thickness could create cracks that would further reduce proton conduction. This optimal thickness was consistent with the results of the through-plane conductivity measurements presented previously. At 100-105 μm , a further increase in thickness no longer contributed significantly to ion conductivity. Any further increase in the thickness would negatively affect the overall sensor performance. Beyond 150 - 160 μm , the performance became worse than the thinnest membranes. This indicated a fine balance between mechanical properties of the membrane and the proton transport characteristics that are directly related to the thickness.

4.4.2. Acid Doping Concentration

The effects of acid doping concentrations on fuel cell sensor performance was examined next. The membrane thickness was kept at 100 - 105 μ m, the optimal thickness obtained from the previous experiments. Moreover, the same acid doping concentrations (i.e. 2, 5 and 10M) for the conductivity test were used to test the fuel cell sensor performance. Lastly, the same membranes used in the conductivity test were used to fabricate the MEAs to maintain consistency. Other parameters were also maintained as before, i.e. 620 ppmv acetone and 140°C. Figure 4-10 summarizes the fuel cell sensor results at the on different acid doping concentrations.



*Figure 4-10: Fuel Cell Sensor Performance at 620ppm Acetone;
Membrane Thickness = 100 - 105 μ m, Temperature = 140°C*

At 2M H₃PO₄, both sPBI and pPBI performed poorly even though the previously studied conductivity of pPBI at this level was much better than sPBI. The sensor performances were abnormally low and very close to the background signal produced by fuel cell sensors. This suggested that not enough H₃PO₄ was present within the PBI backbone to provide effective ion

conduction during the operation. Without ions, the electrochemical circuit cannot be completed and signals cannot be produced. At 5 and 10M H_3PO_4 , both sPBI and pPBI performed substantially better than at 2M. Furthermore, the pPBI outperformed sPBI at both these concentration levels. The 5M doping level was found to yield the best fuel cell sensor performance. While the conductivities of the PBI membranes were the same at 5 and 10M, higher acid concentrations have been shown to negatively affect the mechanical strength of the membrane and in turn fuel cell performance. During the MEA fabrication, the effects of higher temperature and pressure were investigated. This transformation from membranes to MEA might have exacerbated the negative effect induced by an elevated acid concentration. Although this is the most likely cause, more EIS tests on the MEAs are needed to confirm this hypothesis.

4.4.3. Temperature

The final fuel cell sensor study was to determine the effects of temperature. With other conditions maintained at the previously optimal levels. The acid concentration was kept at 5M which was the optimal level found at the previous acid doping study. Figure 4-11 summarizes the data for this fuel cell sensor test.

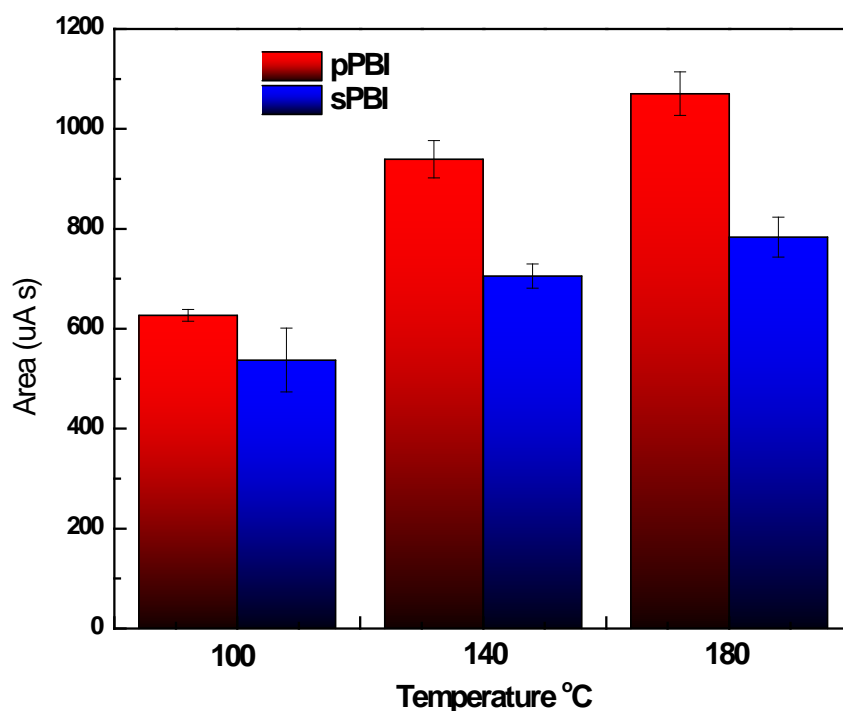


Figure 4-11: Fuel Cell Sensor Performance at 620ppm Acetone; Membrane Thickness = 100 - 105um, Acid Concentration = 5M H_3PO_4

The test results showed that performance increased with temperature. An increase in by temperature 40 degrees should increase the reaction kinetics substantially based on the Arrhenius principle. The results suggest the increase in reaction kinetics outweighs the contribution of the membrane conductivity. pPBI outperformed the sPBI MEAs at all temperatures. Based on this result, the optimized temperature should be 180°C. However, after testing at 180°C, the MEA structure was compromised greatly. Figure 4-12 shows a comparison between two MEAs of the same thickness that were tested at 140°C and 180°C. The MEA tested

at 180°C no longer maintained a flat profile. Instead, it showed wavelike deformations especially at the edge of the MEA. The GDEs also showed signs of detachment from the MEA. Thus, 180°C was deemed unreliable for further sensor tests.

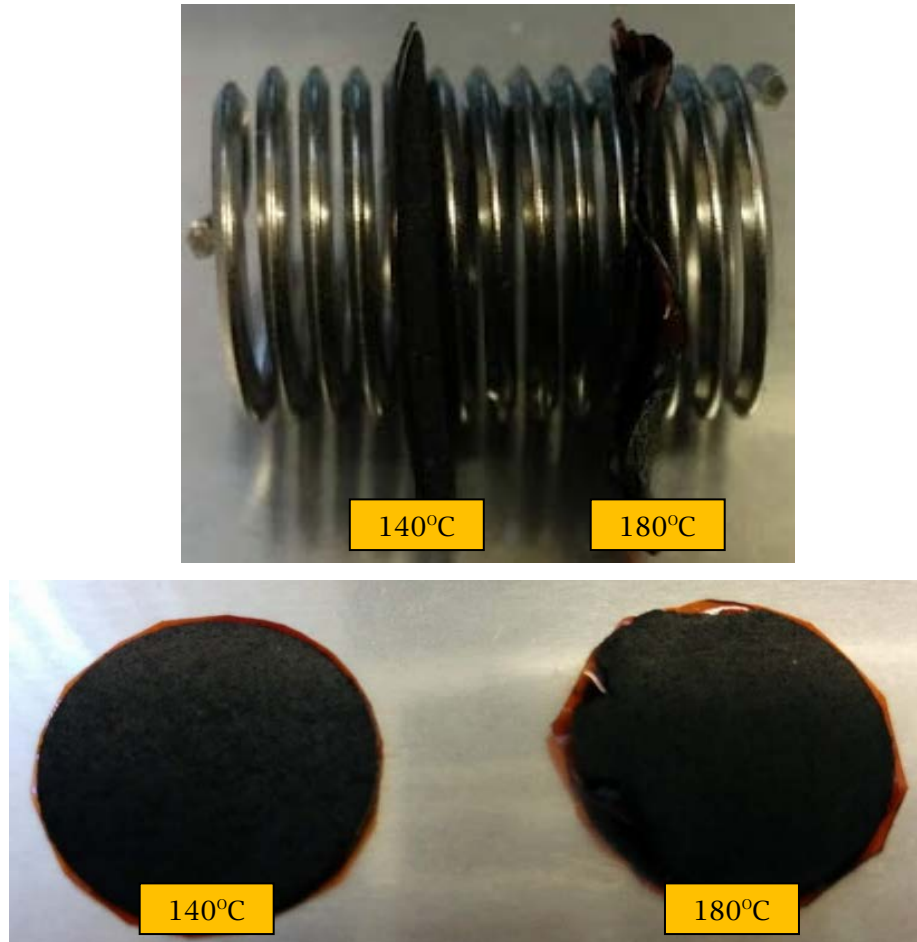


Figure 4-12: MEA Condition After Testing at 140°C (right) and 180°C (left); Membrane Thickness = 103µm

4.4.4. Sensitivity, Detection Limit and Selectivity

Having optimized some of the design features of the examined the sensitivity (linearity), detection limit, and selectivity of the sensors. These three characteristics are important to determine the feasibility of the fuel cell sensor at a proof-of-concept stage.

4.4.4.1. Sensitivity Analysis

The sensitivity study was conducted by testing the best performing MEA at the optimal operating parameters informed by our previous optimization experiments. The MEA was tested for a range of acetone vapour concentrations between 0 and 620 ppmv (in water vapour saturated air). Figure 4-13 summarizes the response curves and the resulting area-concentration calibration curves for the two types of sensors.

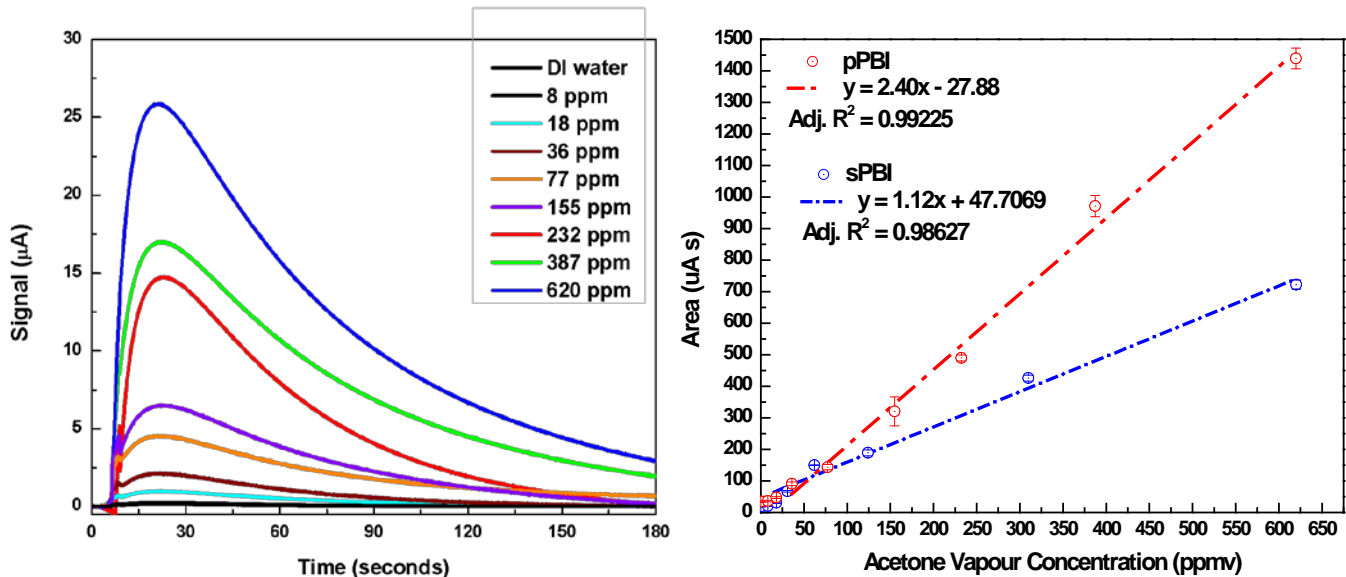


Figure 4-13: Sensitivity Study of the 100um sPBI and pPBI MEA at 140°C; Acid Doping Concentration = 5M. Left: Response Curves; Right: Linearity

Both pPBI and sPBI exhibited a linear relationship between the curve areas and the acetone concentration. Linear regressions on sPBI and pPBI produced adjusted R^2 values of 0.98627 and 0.99225. The slope of this linear relationship represents the sensitivity of the fuel cell sensor. This value represents how much the curve area changes as a response to a change in the acetone concentration. Thus, from the slopes in Figure 4-13, pPBI was more than twice as sensitive as sPBI for detection of acetone. The linear sensitivity of the fuel cell sensor extended over a much larger range than do the SMO acetone sensors. SMO acetone gas sensors only exhibited linear sensitivity over narrow concentration range, if at all. The vast majority of SMO gas sensors reported in the literature showed a linear relationship only between 0 – 100ppmv [86], [87], [96], [88]–[95]. Furthermore, different SMO material designs and morphologies produced completely different sensitivity relationships. This made comparison of the SMO sensors difficult. In contrast, fuel cell sensors usually yield a linear relationship between their responses and the analyte concentration, as demonstrated in the alcohol sensing industry and literature [18]. SMO sensors measure the acetone concentration indirectly through the changes in the material electrical properties. This change in electrical properties tends to diminishing as the acetone concentration increase. Fuel cell sensors determine the amount of acetone concentration directly by measuring the number of electrons passing through the circuit as the electrochemical reaction occur. This difference these the detection mechanisms explains why the response of the fuel cell sensor remained linear over a large range while the SMO sensors' range was much more limited.

Obviously, a linear sensitivity is preferred over a non-linear one. As the sensors age and undergo many operation cycles, the sensor response will inevitably be affected and so it must be recalibrated. A sensor with a detection mechanism that guarantees a linear calibration curve would be the most reliable. A sensor with nonlinear response relative to the target analyte concentration would be difficult to calibrate.

4.4.4.2. Detection Limit

In theory, area-concentration calibration curves should pass through the origin. However, in real cases, interferences and background noises are unavoidable. These interferences and noises are the biggest restrictions to achieve a low detection limit. To determine the detection limit or the limit range, the sensor response at low acetone concentrations was examined. Figure 4-14 shows a low acetone concentration portions of the calibration curves appearing in Figure 4-13.

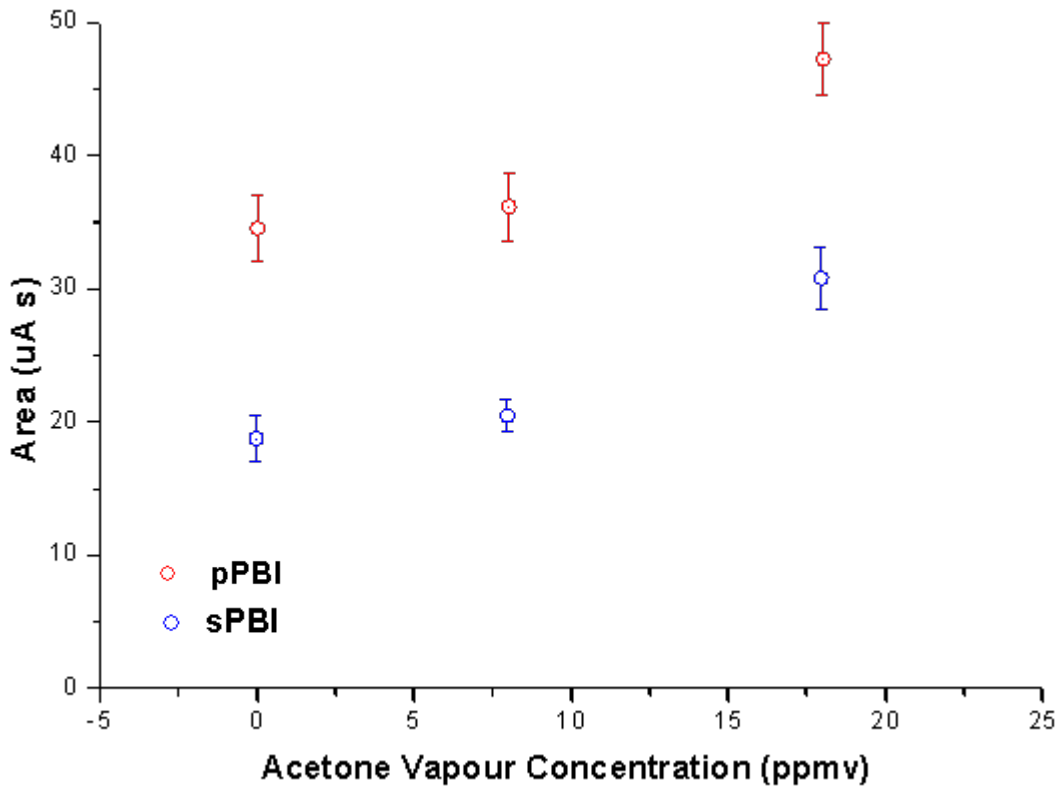


Figure 4-14: Low Acetone Concentration Sensor Responses with sPBI and pPBI

Three data points corresponding to the sensor response at 0, 8 and 16 ppmv for both pPBI and sPBI are shown. In each case, the responses at 0 and 8 ppmv were statistically indistinguishable, which suggests that the sensor cannot detect acetone concentrations lower than 8ppmv. Accounting for the response errors, the detection limit is likely higher than 12 ppmv. The sensor response at 16ppmv produced a statistically higher response than 0 and 8 ppmv. Thus, a realistic detection limit of both sPBI and pPBI would be in the range of 15-20 ppmv acetone.

Compared to SMO acetone gas sensors, the detection limit of the fuel cell gas sensor was still far away from what SMO based sensor can achieve. As mentioned in Chapter 1.1, an SMO acetone gas sensor detects concentrations as low as 50ppb acetone. The fuel cell sensor used in this work is a commercial one with only 0.5 mg Pt/cm² catalyst. To raise the detection limit, the sensor response and sensitivity must be increased. This can be achieved by raising the catalyst loading. Another issue to be addressed in order to improve the detection limit was the background noise. The water (zero ppmv acetone) response from the pPBI was higher than that of sPBI. Furthermore, an improvement in the sensor response may also increase the noise at lower concentrations. If noise cannot be isolated and/or controlled, it will hinder further efforts in lowering the detection limit.

4.4.4.3. Selectivity

The selectivity study was also carried out with the same MEA used in the sensitivity test. Besides acetone, methanol and ethanol were also used. Methanol and ethanol are the most abundant chemicals in human breath, as well as being key analytes in food monitoring and packaging applications [3], [4], [97]. The sensor was tested with each analyte at a vapour concentration of 600ppmv. The MEA was tested with one analyte, then stored in the acid chamber overnight before another analyte was tested. This was done to eliminate possible confounding effects had all the analytes been tested back-to-back. Figure 4-15 summarizes the responses of both sPBI and pPBI sensor responses to 600ppmv of acetone, ethanol and methanol.

The results demonstrated that the fuel cell had a moderate degree of selectivity toward acetone. At the same analyte concentration, the response sPBI ratio between acetone/methanol and acetone/ethanol were 1.47 and 2.04, respectively. For pPBI, the ratios were 2.13 and 3.18. SMO gas sensor literatures reported ratios between acetone responses and other VOCs including methanol and ethanol ranging from 1 to 20 [6]-[9], [12], [13], [15], [16]. This puts the fuel cell sensor at the lower end of the selectivity spectrum among acetone gas sensors. The lower selectivity ratio was due to the use of a commercial GDE which was not designed for selectivity. While the selectivity of the fuel cell sensor is relatively low, the fact that the sensor could achieve

some level of selectivity was very promising. Further work on the catalyst to enhance the selectivity of the fuel cell sensor is needed.

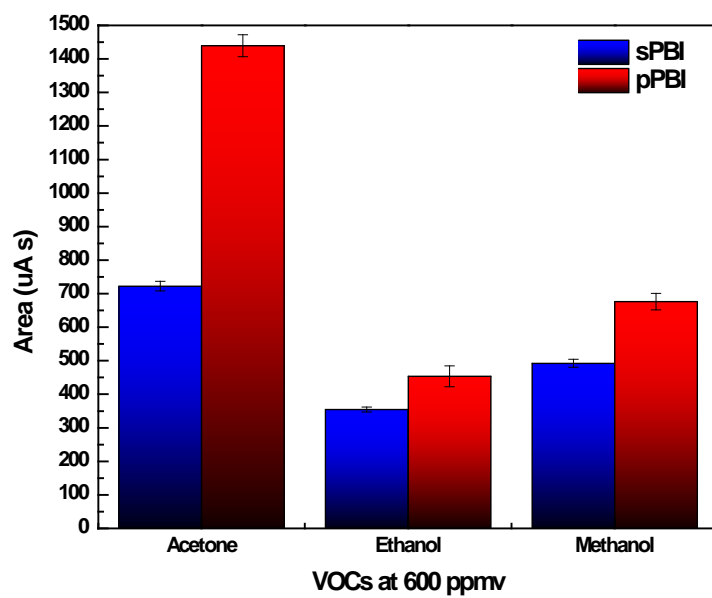


Figure 4-15: pPBI and sPBI Sensor Reponse for Acetone, Ethanol and Methanol at 600ppmv

5. Conclusions and Recommendations

5.1. Summary

Currently, much research effort is aimed toward developing SMO acetone gas sensors to match the increased demand for inexpensive, sensitive and reliable sensing for many applications. While SMO gas sensors are easy to fabricate and operate and have low detection limits, they still have critical downsides such as high operating temperatures, intricate material synthesis and complex sensitivity relationships. To date, exists little has been reported about fuel cell gas sensors. Thus, a genuine interest in exploring other alternatives. In this work, a simple phosphoric acid-based acetone gas fuel cell sensor was fabricated and evaluated to explore its feasibility as an alternative to SMO gas sensors. The fuel cell sensor was constructed with a commercially available GDE and PBI membrane with two distinct morphologies: solid and porous. An automated testing system and a custom fuel cell housing were designed to evaluate the membranes and fuel cell sensors.

For the fuel cell, two PBI membrane morphologies were studied in detail for the dependence of conductivity on membrane thickness, acid doping concentration and operating temperature. Then, fuel cell sensor tests were carried out based on the optimized membrane parameters to determine the ideal operating conditions. MEAs made from membranes with thicknesses between 100 – 105 μm , doped at 5M H_3PO_4 and operated at 140°C proved to be the best sensors. At 180°C, the initial performance was better than that at 140°C, but the heat stress degraded the mechanical integrity of the MEA. This applied for both membrane morphologies. The fuel cell sensors showed a consistent linear response relationship over a wide range of acetone concentration which was more desirable than their SMO alternatively. However, the detection limit and the selectivity were not as promising. Part of this can be explained by the inherent limitations with commercial fuel cell catalysts coupled with a low catalyst loading. Overall, this work has demonstrated the proof-of-concept that fuel cell sensors can detect

acetone gas with a superior sensitivity to SMOs. More improvements are required to lower the detection limit.

5.2. Recommendations

While this work has focused on the effect of the membrane on sensor performance, no attention was paid to the catalyst. Improvements can be made by incorporating the SMO research on this topic. Tungsten oxide (WO_2) has emerged as one of the most selective thermal oxidation catalyst toward acetone [12], [14], [98], [99]. If the GDE can be designed to incorporate both WO_3 along with carbon-supported Pt, this may increase not only the selectivity, but also the sensitivity of the fuel cell gas sensor. Kim et al. functionalized Pt with WO_3 hemitubes to detect acetone with much success [9]. Employing oxides with high affinity to acetone adsorption can also improve the sensitivity and selectivity [100], [101].

This work only focused on the initial fuel cell sensor performance. Long term stability is another important characteristic. Commercial gas sensors typically have a minimum calibration cycle of 12 months and up to 5 years. Thus, depending on the application and the error tolerance, the fuel cell gas sensor must to be evaluated for its effectiveness over long periods of time and many operating cycles. Common problems with acid-doped membranes, such as acid leaching and membrane degradation in sensing application, also must be investigated.

Our experiments have shown that the best sensing response is obtained at 180°C. However, the MEA mechanically degraded after being tested at this condition. Higher temperatures can promote faster kinetics and therefore improve sensor sensitivity and detection limit. Efforts should be spent into solving this mechanical issue when operating at the higher temperature. Longer chain PBI can be employed to produce more stable and robust membranes that can handle higher temperature. Furthermore, additives such as graphene, PTFE and many others have been shown to improve not only the mechanical properties but also fuel cell sensor performance in a variety of polymer membrane composites [18], [74] [102], [103]. The GDE adhesive coating might also be a problem. Nafion is not a good candidate for this application.

The higher operating temperature will dehydrate a Nafion layer and drastically increase the interfacial resistance between the GDE and the membranes. Thus, PBI can be directly used for this purpose. However, the MEA fabrication process must be tuned correctly. The hot press temperature and pressure must be high enough for the PBI molecules in the GDE to bond strongly to the membrane. But if the temperature and pressure are too high, the MEA will instead be damaged. Many avenues for improvements are possible for to this proof-of-concept. However, the added cost to the sensor by implementing these improvements cannot be neglected as manufacturing costs is a key requirement for commercial viability.

References

- [1] Z. Yunusa, M. N. Hamidon, A. Kaiser, and Z. Awang, "Gas Sensors : A Review," *Sensors and Transducers*, vol. 168, no. 4, pp. 61–75, 2014.
- [2] A. Dey, "Semiconductor metal oxide gas sensors: A review," *Mater. Sci. Eng. B Solid-State Mater. Adv. Technol.*, vol. 229, no. July 2017, pp. 206–217, 2018.
- [3] V. Saasa, T. Malwela, M. Beukes, M. Mokgotho, C.-P. Liu, and B. Mwakikunga, "Sensing Technologies for Detection of Acetone in Human Breath for Diabetes Diagnosis and Monitoring," *Diagnostics*, vol. 8, no. 1, p. 12, 2018.
- [4] V. Galstyan, M. P. B. Id, and V. Sberveglieri, "Metal Oxide Nanostructures in Food Applications : Quality Control and Packaging," pp. 1–21, 2018.
- [5] G. Korotcenkov and B. K. Cho, "Metal oxide composites in conductometric gas sensors: Achievements and challenges," *Sensors Actuators, B Chem.*, vol. 244, pp. 182–210, 2017.
- [6] L. Liu, S. Li, J. Zhuang, L. Wang, J. Zhang, H. Li, Z. Liu, Y. Han, X. Jiang, and P. Zhang, "Improved selective acetone sensing properties of Co-doped ZnO nanofibers by electrospinning," *Sensors Actuators, B Chem.*, vol. 155, no. 2, pp. 782–788, 2011.
- [7] J. W. Yoon, J. S. Kim, T. H. Kim, Y. J. Hong, Y. C. Kang, and J. H. Lee, "A New Strategy for Humidity Independent Oxide Chemiresistors: Dynamic Self-Refreshing of In₂ O₃ Sensing Surface Assisted by Layer-by-Layer Coated CeO₂ Nanoclusters," *Small*, vol. 12, no. 31, pp. 4229–4240, 2016.
- [8] F. Qu, Y. Yuan, R. Guarecuco, and M. Yang, "Low Working-Temperature Acetone Vapor Sensor Based on Zinc Nitride and Oxide Hybrid Composites," *Small*, vol. 12, no. 23, pp. 3128–3133, 2016.
- [9] S. J. Choi, I. Lee, B. H. Jang, D. Y. Youn, W. H. Ryu, C. O. Park, and I. D. Kim, "Selective diagnosis of diabetes using Pt-functionalized WO₃ hemitube networks as a sensing layer

- of acetone in exhaled breath,” *Anal. Chem.*, vol. 85, no. 3, pp. 1792–1796, 2013.
- [10] J. S. Jang, S. J. Choi, S. J. Kim, M. Hakim, and I. D. Kim, “Rational Design of Highly Porous SnO₂ Nanotubes Functionalized with Biomimetic Nanocatalysts for Direct Observation of Simulated Diabetes,” *Adv. Funct. Mater.*, vol. 26, no. 26, pp. 4740–4748, 2016.
- [11] P. Gunawan, L. Mei, J. Teo, J. Ma, J. Highfield, Q. Li, and Z. Zhong, “Ultrahigh sensitivity of Au/1D α -Fe₂O₃ to acetone and the sensing mechanism,” *Langmuir*, vol. 28, no. 39, pp. 14090–14099, 2012.
- [12] M. Righettoni, A. Tricoli, and S. E. Pratsinis, “Si : WO₃ Sensors for Highly Selective Detection of Acetone for Easy Diagnosis of Diabetes by Breath Analysis,” *Anal. Chem.*, vol. 82, no. 9, pp. 3581–3587, 2010.
- [13] Y. J. Jeong, W.-T. Koo, J.-S. Jang, D.-H. Kim, M.-H. Kim, and I.-D. Kim, “Nanoscale PtO₂ Catalysts-Loaded SnO₂ Multichannel Nanofibers toward Highly Sensitive Acetone Sensor,” *ACS Appl. Mater. Interfaces*, vol. 10, no. 2, pp. 2016–2025, 2018.
- [14] J. Y. Shen, M. Di Wang, Y. F. Wang, J. Y. Hu, Y. Zhu, Y. X. Zhang, Z. J. Li, and H. C. Yao, “Iron and carbon codoped WO₃ with hierarchical walnut-like microstructure for highly sensitive and selective acetone sensor,” *Sensors Actuators, B Chem.*, vol. 256, pp. 27–37, 2018.
- [15] C. Wang, J. Liu, Q. Yang, P. Sun, Y. Gao, F. Liu, J. Zheng, and G. Lu, “Ultrasensitive and low detection limit of acetone gas sensor based on W-doped NiO hierarchical nanostructure,” *Sensors Actuators, B Chem.*, vol. 220, pp. 59–67, 2015.
- [16] R. K. Mishra, G. Murali, T.-H. Kim, J. H. Kim, Y. J. Lim, B.-S. Kim, P. P. Sahay, and S. H. Lee, “Nanocube In₂O₃@RGO heterostructure based gas sensor for acetone and formaldehyde detection,” *RSC Adv.*, vol. 7, no. 61, pp. 38714–38724, 2017.
- [17] K. Xu, C. Fu, Z. Gao, F. Wei, Y. Ying, C. Xu, and G. Fu, “Nanomaterial-based gas sensors: A review,” *Instrum. Sci. Technol.*, vol. 9149, pp. 1–31, 2017.

- [18] J. Leno, "Improved Environmental Operation of Alcohol Breathalyzers with Functionalized Graphene Nanocomposite Membranes," University of Waterloo, 2016.
- [19] M. J. McGrath, C. N. Scanaill, and D. Nafus, *Sensor Technologies: Healthcare, Wellness and Environmental Applications*. Apress Open, 2013.
- [20] PrimeBreathalyzers, "Breathalyzer Sensor Technologies." [Online]. Available: <http://www.primebreathalyzers.com/fuel-cell-vs-semiconductor-sensor>.
- [21] A. H. Jalal, Y. Umasankar, M. Chowdhury, and S. Bhansali, "A Fuel Cell Sensing Platform for Selective Detection of Acetone in Hyperglycemic Patients," *Meet. Abstr.*, vol. MA2017-02, no. 50, pp. 2130-2130, 2017.
- [22] A. Chandan, M. Hattenberger, A. El-Kharouf, S. Du, A. Dhir, V. Self, B. G. Pollet, A. Ingram, and W. Bujalski, "High temperature (HT) polymer electrolyte membrane fuel cells (PEMFC)- A review," *J. Power Sources*, vol. 231, pp. 264-278, 2013.
- [23] C. Xu, X. Liu, J. Cheng, and K. Scott, "A polybenzimidazole/ionic-liquid-graphite-oxide composite membrane for high temperature polymer electrolyte membrane fuel cells," *J. Power Sources*, vol. 274, pp. 922-927, 2015.
- [24] N. Z. Hausmann, "Toward the design of an enzymatic breath sensor for acetone and the directed assembly of enzymes on comb-branched DNA," Saint Louis University, 2013.
- [25] L. M. Haverhals, "Fuel cells as Power Sources and Sensors," 2008.
- [26] C. Qin, J. Wang, D. Yang, B. Li, and C. Zhang, "Proton Exchange Membrane Fuel Cell Reversal: A Review," *Catalysts*, vol. 6, no. 12, p. 197, 2016.
- [27] W. R. W. Daud, R. E. Rosli, E. H. Majlan, S. A. A. Hamid, R. Mohamed, and T. Husaini, "PEM fuel cell system control: A review," *Renew. Energy*, vol. 113, pp. 620-638, 2017.
- [28] X. Wu and K. Scott, "A H₂SO₄ loaded polybenzimidazole (PBI) membrane for high temperature PEMFC," *Fuel Cells*, vol. 12, no. 4, pp. 583-588, 2012.

- [29] J.-P. Melchior, G. Majer, and K.-D. Kreuer, "Why do proton conducting polybenzimidazole phosphoric acid membranes perform well in high-temperature PEM fuel cells?," *Phys. Chem. Chem. Phys.*, vol. 19, no. 1, pp. 601-612, 2017.
- [30] Y. Shao, G. Yin, Z. Wang, and Y. Gao, "Proton exchange membrane fuel cell from low temperature to high temperature: Material challenges," *J. Power Sources*, vol. 167, no. 2, pp. 235-242, 2007.
- [31] C. Pan, R. He, Q. Li, J. O. Jensen, N. J. Bjerrum, H. A. Hjulmand, and A. B. Jensen, "Integration of high temperature PEM fuel cells with a methanol reformer," *J. Power Sources*, vol. 145, no. 2, pp. 392-398, 2005.
- [32] M. A. Haque, A. B. Sulong, K. S. Loh, E. H. Majlan, T. Husaini, and R. E. Rosli, "Acid doped polybenzimidazoles based membrane electrode assembly for high temperature proton exchange membrane fuel cell: A review," *Int. J. Hydrogen Energy*, vol. 30, pp. 1-24, 2015.
- [33] J.-M. Bae, I. Honma, M. Murata, T. Yamamoto, M. Rikukawa, and N. Ogata, "Properties of selected sulfonated polymers as proton-conducting electrolytes for polymer electrolyte fuel cells," *Solid State Ionics*, vol. 147, no. 1-2, pp. 189-194, 2002.
- [34] D. J. Jones and J. Rozière, "Recent advances in the functionalisation of polybenzimidazole and polyetherketone for fuel cell applications," *J. Memb. Sci.*, vol. 185, no. 1, pp. 41-58, 2001.
- [35] Q. Li, R. He, J. O. Jensen, and N. J. Bjerrum, "Approaches and Recent Development of Polymer Electrolyte Membranes for Fuel Cells Operating above 100 °C," *Chem. Mater.*, vol. 15, no. 26, pp. 4896-4915, 2003.
- [36] N. J. Leonard, "Carl Shipp Marvel - A Biographical Memoir by Nelson J. Leonard." National Academy of Science, p. 34, 1994.
- [37] Q. Li, R. He, J. O. Jensen, and N. J. Bjerrum, "PBI-Based Polymer Membranes for High Temperature Fuel Cells - Preparation, Characterization and Fuel Cell Demonstration," *Fuel*

- Cells*, vol. 4, no. 3, pp. 147–159, 2004.
- [38] M. Y. Sen and J. E. Puskas, “Doping Phosphoric Acid in Polybenzimidazole Membranes for High Temperature Proton Exchange Membrane Fuel Cells,” *Am. Chem. Soc. Polym. Prepr. Div. Polym. Chem.*, vol. 49, no. 1, pp. 487–488, 2008.
 - [39] X. BZ and O. Savadogo, “The effect of acid doping on the conductivity of polybenzimidazole (PBI),” *J. New Mater. Electrochem. Syst.*, vol. 2, no. 2, pp. 95–101, 1999.
 - [40] B. Xing and O. Savadogo, “Hydrogen/oxygen polymer electrolyte membrane fuel cell (PEMFC) based on acid-doped polybenzimidazole (PBI),” *J. New Mater. Electrochem. Syst.*, vol. 3, no. 4, pp. 343–347, 2000.
 - [41] X. Wu and K. Scoot, “A H₂SO₄ Loaded Polybenzimidazole (PBI) Membrane for High Temperature PEMFC,” *Fuel Cells*, vol. 12, no. 4, pp. 583–588, 2012.
 - [42] A. Carollo, E. Quartarone, C. Tomasi, P. Mustarelli, F. Belotti, A. Magistris, F. Maestroni, M. Parachini, L. Garlaschelli, and P. P. Righetti, “Developments of new proton conducting membranes based on different polybenzimidazole structures for fuel cells applications,” *J. Power Sources*, vol. 160, no. 1, pp. 175–180, 2006.
 - [43] J. . Holladay, J. . Wainright, E. . Jones, and S. . Gano, “Power generation using a mesoscale fuel cell integrated with a microscale fuel processor,” *J. Power Sources*, vol. 130, no. 1–2, pp. 111–118, 2004.
 - [44] J. A. Kerres, “Development of ionomer membranes for fuel cells,” *J. Memb. Sci.*, vol. 185, no. 1, pp. 3–27, 2001.
 - [45] J.-T. Wang, R. Savinell, J. Wainright, M. Litt, and H. Yu, “A H₂O₂ fuel cell using acid doped polybenzimidazole as polymer electrolyte,” *Electrochim. Acta*, vol. 43, pp. 193–197, 1996.
 - [46] T. Toda, H. Igarashi, H. Uchida, and M. Watanabe, “Enhancement of the Electroreduction of Oxygen on Pt Alloys with Fe, Ni, and Co,” *J. Electrochem. Soc.*, vol. 146, no. 10, pp. 3750–

3756, 1999.

- [47] E. Antolini, J. R. C. Salgado, and E. R. Gonzalez, "The stability of Pt-M (M = first row transition metal) alloy catalysts and its effect on the activity in low temperature fuel cells: A literature review and tests on a Pt-Co catalyst," *J. Power Sources*, vol. 160, no. 2, pp. 957-968, 2006.
- [48] U. A. Paulus, A. Wokaun, G. G. Scherer, T. J. Schmidt, V. Stamenkovic, N. M. Markovic, and P. N. Ross, "Oxygen reduction on high surface area Pt-based alloy catalysts in comparison to well defined smooth bulk alloy electrodes," *Electrochim. Acta*, vol. 47, no. 22-23, pp. 3787-3798, 2002.
- [49] F. Mack, M. Klages, J. Scholta, L. Jörisen, T. Morawietz, R. Hiesgen, D. Kramer, and R. Zeis, "Morphology studies on high-temperature polymer electrolyte membrane fuel cell electrodes," *J. Power Sources*, vol. 255, pp. 431-438, 2014.
- [50] Eva Novillo, M. Pardo, and A. García-Luis, "Novel Approaches for the Integration of High Temperature PEM Fuel Cells Into Aircrafts," *J. Fuel Cell Sci. Technol*, vol. 8, no. 1, pp. 11-14, 2010.
- [51] Z.-M. Zhou, Z.-G. Shao, X.-P. Qin, X.-G. Chen, Z.-D. Wei, and B.-L. Yi, "Durability study of Pt-Pd/C as PEMFC cathode catalyst," *Int. J. Hydrogen Energy*, vol. 34, no. 4, pp. 1719-1726, 2010.
- [52] Y. Shao, G. Yin, and Y. Gao, "Understanding and approaches for the durability issues of Pt-based catalysts for PEM fuel cell," *J. Power Sources*, vol. 171, no. 2, pp. 558-566, 2007.
- [53] C. Venkateswara, R. Javier, P. Sundara, L. Ghatti, and B. Rambabu, "High temperature polymer electrolyte membrane fuel cell performance of Pt/C cathodes," *J. Power Sources*, vol. 195, no. 11, pp. 3425-3430, 2010.
- [54] M. Mamlouk, J. H. Jang, and K. Scott, "Intermediate Temperature Fuel Cell and Oxygen Reduction Studies With Carbon-Supported Platinum Alloy Catalysts in Phosphoric Acid

- Based Systems,” *J. Fuel Cell Sci. Technol*, vol. 9, no. 1, pp. 2–9, 2011.
- [55] C. Oettel, L. Rihko-Struckmann, and K. Sundmacher, “Improved CO Tolerance With PtRu Anode Catalysts in ABPBI Based High Temperature Proton Exchange Membrane Fuel Cells,” *J. Fuel Cell Sci. Technol*, vol. 9, no. 3, p. 7, 2012.
- [56] C. Song, S. (Rob) Hui, and J. Zhang, *High-temperature PEM Fuel Cell Catalysts and Catalyst Layers*. London: Springer, 2008.
- [57] Q. Li, D. Aili, H. . Hjuler, and J. . Jensen, *High temperature polymer electrolyte membrane fuel cells: approaches, status, and perspectives*. Springer, 2015.
- [58] L. J. Bonville, H. R. Kunz, Y. Song, A. Mientek, M. Williams, A. Ching, and J. M.Fenton, “Development and demonstration of a higher temperature PEM fuel cell stack,” *J. Power Sources*, vol. 144, no. 1, pp. 107–112, 2005.
- [59] W. Bujalski, A. Chandan, M. Hattenberger, A. El-kharouf, S. Du, A. Dhir, V. Self, B. G. Pollet, A. Ingram, and W. Bujalski, “High temperature (HT) polymer electrolyte membrane fuel cells (PEMFC) – A review,” *J. Power Sources*, vol. 231, pp. 264–278, 2013.
- [60] H.-J. Lee, B. G. Kim, D. H. Lee, S. J. Park, Y. Kim, J. W. Lee, D. Henkensmeier, S. W. Nam, H.-J. Kim, H. Kim, and J.-Y. Kim, “Demonstration of a 20 W class high-temperature polymer electrolyte fuel cell stack with novel fabrication of a membrane electrode assembly,” *Int. J. Hydrogen Energy*, vol. 36, no. 9, pp. 5521–5526, 2011.
- [61] X. Li, “Structure-Property Relationships in Polybenzimidazole Materials for Gas Separation and Fuel Cell Applications,” 2014.
- [62] M. Montalvillo, V. Silva, L. Palacio, J. Calvo, F. Carmona, A. Hernández, and P. Prádanos, “Charge and dielectric characterization of nanofiltration membranes by impedance spectroscopy,” *J Membr Sci*, vol. 454, pp. 163–173, 2014.
- [63] M. Montalvillo, V. Silva, L. Palacio, A. Hernández, and P. Prádanos, “Dielectric properties of

- electrolyte solutions in polymeric nanofiltration membranes,” *Desalin. Water Treat.*, vol. 27, no. 1-3, pp. 25-30, 2011.
- [64] J.-S. Park, J.-H. Choi, K.-H. Yeon, and S.-H. Moon, “An approach to fouling characterization of an ion-exchange membrane using current-voltage relation and electrical impedance spectroscopy,” *J Colloid Interface Sci*, vol. 294, pp. 129-138, 2006.
- [65] J. Kavanagh, S. Hussain, T. Chilcott, and H. Coster, “Fouling of reverse osmosis membranes using electrical impedance spectroscopy: measurements and simulations,” *Desalination*, vol. 236, pp. 187-193, 2009.
- [66] Z. Hu, A. Antony, G. Leslie, and P. Le-Clech, “Real-time monitoring of scale formation in reverse osmosis using electrical impedance spectroscopy,” *J Membr Sci*, vol. 453, pp. 320-237, 2014.
- [67] D. J. Stokes, *Principles and Practice of Variable Pressure Environmental Scanning Electron Microscopy (VP-ESEM)*. Chichester: John Wiley & Sons, 2008.
- [68] R. Saravanan, “Method for Building a Fuel Cell,” in *Materials for Fuel Cells*, 1st ed., 2008, pp. 213-220.
- [69] U.S. Secretary of Commerce, *NIST Chemistry WebBook, SRD 69*. 2017.
- [70] H.-J. Benkelberg, S. Hamm, and R. Warnec, “Henry’s Law Coefficients for Aqueous Solutions of Acetone, Acetaldehyde and Acetonitrile, and Equilibrium Constants for the Addition Compounds of Acetone and Acetaldehyde with Bisulfite,” *J. Atmos. Chem.*, vol. 20, pp. 17-34, 1995.
- [71] Y.-L. Ma, J. S. Wainright, M. H. Litt, and R. F. Savinell, “Conductivity of PBI Membranes for High-Temperature Polymer Electrolyte Fuel Cells,” *J. Electrochem. Soc.*, vol. 151, p. A8, 2004.
- [72] O. Savadogo and B. Xing, “Hydrogen/oxygen polymer electrolyte membrane fuel cell

- (PEMFC) based on acid-doped polybenzimidazole (PBI)," *J. New Mater. Electrochem. Syst.*, vol. 3, no. 4, pp. 343–347, 2000.
- [73] Q. Li, R. He, R. W. Berg, H. A. Hjuler, and N. J. Bjerrum, "Water uptake and acid doping of polybenzimidazoles as electrolyte membranes for fuel cells," *Solid State Ionics*, vol. 168, no. 1-2, pp. 177–185, 2004.
- [74] H. L. Lin, Y. C. Chen, C. C. Li, C. P. Cheng, and T. L. Yu, "Preparation of PBI/PTFE composite membranes from PBI in N,N'-dimethyl acetamide solutions with various concentrations of LiCl," *J. Power Sources*, vol. 181, no. 2, pp. 228–236, 2008.
- [75] R. He, Q. Li, G. Xiao, and N. J. Bjerrum, "Proton conductivity of phosphoric acid doped polybenzimidazole and its composites with inorganic proton conductors," *J. Memb. Sci.*, vol. 226, no. 1-2, pp. 169–184, 2003.
- [76] E. Harikishan Reddy and S. Jayanti, "Thermal management strategies for a 1 kWe stack of a high temperature proton exchange membrane fuel cell," *Appl. Therm. Eng.*, vol. 48, pp. 465–475, 2012.
- [77] J. S. Yang, L. N. Cleemann, T. Steenberg, C. Terkelsen, Q. F. Li, J. O. Jensen, H. A. Hjuler, N. J. Bjerrum, and R. H. He, "High molecular weight polybenzimidazole membranes for high temperature PEMFC," *Fuel Cells*, vol. 14, no. 1, pp. 7–15, 2014.
- [78] Q. Li, R. He, J. O. Jensen, and N. J. Bjerrum, "PBI-based polymer membranes for high temperature fuel cells - Preparation, characterization and fuel cell demonstration," *Fuel Cells*, vol. 4, no. 3, pp. 147–159, 2004.
- [79] F. Mack, K. Aniol, C. Ellwein, J. Kerres, and R. Zeis, "Novel phosphoric acid-doped PBI-blends as membranes for high-temperature PEM fuel cells," *J. Mater. Chem. A*, vol. 3, no. 20, pp. 10864–10874, 2015.
- [80] Y. H. Jeong, J. H. Jung, E. Choi, S. Han, A. I. Begley, S. J. Yoo, J. H. Jang, H. J. Kim, S. W. Nam, K. Y. Lee, and J. Y. Kim, "Colorimetric determination of phosphoric acid leakage for

- phosphoric acid-doped polybenzimidazole membrane fuel cell applications,” *J. Power Sources*, vol. 299, pp. 480–484, 2015.
- [81] K. Hwang, J. H. Kim, S. Y. Kim, and H. Byun, “Preparation of polybenzimidazole-based membranes and their potential applications in the fuel cell system,” *Energies*, vol. 7, no. 3, pp. 1721–1732, 2014.
- [82] J. Mader, L. Xiao, T. J. Schmidt, and B. C. Benicewicz, *Advances in Polymer Science*. 2008.
- [83] M.-Q. Li, Z.-G. Shao, and K. Scott, “A high conductivity Cs_{2.5}H_{0.5}PMo₁₂O₄₀/polybenzimidazole (PBI)/H₃PO₄ composite membrane for proton-exchange membrane fuel cells operating at high temperature,” *J. Power Sources*, vol. 183, no. 1, pp. 69–75, 2008.
- [84] M. Li and K. Scott, “A polymer electrolyte membrane for high temperature fuel cells to fit vehicle applications,” *Electrochim. Acta*, vol. 55, no. 6, pp. 2123–2128, 2010.
- [85] T. Michot, A. Nishimoto, and M. Watanabe, “Electrochemical properties of polymer gel electrolytes based on poly(vinylidene fluoride) copolymer and homopolymer,” *Electrochim. Acta*, vol. 45, no. 8–9, pp. 1347–1360, 2000.
- [86] A. D. Worrall, Z. Qian, J. A. Bernstein, A. P. Angelopoulos, Q. Qi, T. Zhang, L. Liu, X. Zheng, Q. Yu, Y. Zeng, H. Yang, M. Arvani, H. Mohammad Aliha, A. A. Khodadadi, and Y. Mortazavi, “Water-Resistant Polymeric Acid Membrane Catalyst for Acetone Detection in the Exhaled Breath of Diabetics,” *Anal. Chem.*, vol. 24, no. 6, p. acs.analchem.7b03808, 2018.
- [87] T. I. Nasution, I. Nainggolan, S. D. Hutagalung, K. R. Almad, Z. A. Ahmad, K. R. Ahmad, and Z. A. Ahmad, “The sensing mechanism and detection of low concentration acetone using chitosan-based sensors,” *Sensors Actuators B Chem.*, vol. 177, pp. 522–528, 2013.
- [88] X. Bai, H. Ji, P. Gao, Y. Zhang, and X. Sun, “Morphology, phase structure and acetone sensitive properties of copper-doped tungsten oxide sensors,” *Sensors Actuators, B Chem.*, vol. 193, pp. 100–106, 2014.

- [89] R. C. Biswal, "Pure and Pt-loaded gamma iron oxide as sensor for detection of sub ppm level of acetone," *Sensors Actuators, B Chem.*, vol. 157, no. 1, pp. 183–188, 2011.
- [90] L. L. Deng, C. X. Zhao, Y. Ma, S. S. Chen, and G. Xu, "Low cost acetone sensors with selectivity over water vapor based on screen printed TiO₂ nanoparticles," *Anal. Methods*, vol. 5, no. 15, p. 3709, 2013.
- [91] D. Chen, X. Hou, T. Li, L. Yin, B. Fan, H. Wang, X. Li, H. Xu, H. Lu, R. Zhang, and J. Sun, "Effects of morphologies on acetone-sensing properties of tungsten trioxide nanocrystals," *Sensors Actuators, B Chem.*, vol. 153, no. 2, pp. 373–381, 2011.
- [92] X. L. Xu, Y. Chen, S. Y. Ma, W. Q. Li, and Y. Z. Mao, "Excellent acetone sensor of La-doped ZnO nanofibers with unique bead-like structures," *Sensors Actuators, B Chem.*, vol. 213, pp. 222–233, 2015.
- [93] S. Salehi, E. Nikan, A. A. Khodadadi, and Y. Mortazavi, "Highly sensitive carbon nanotubes-SnO₂ nanocomposite sensor for acetone detection in diabetes mellitus breath," *Sensors Actuators, B Chem.*, vol. 205, pp. 261–267, 2014.
- [94] F. Liu, B. Wang, X. Yang, X. Liang, P. Sun, X. Chuai, Y. Gao, F. Liu, and G. Lu, "Sub-ppm YSZ-based mixed potential type acetone sensor utilizing columbite type composite oxide sensing electrode," *Sensors Actuators B Chem.*, vol. 238, pp. 928–937, 2017.
- [95] K. W. Kao, M. C. Hsu, Y. H. Chang, S. Gwo, and J. Andrew Yeh, "A Sub-ppm acetone gas sensor for diabetes detection using 10 nm thick ultrathin InN FETs," *Sensors (Switzerland)*, vol. 12, no. 6, pp. 7157–7168, 2012.
- [96] J. Luo, S. Y. Ma, F. M. Li, X. B. Li, W. Q. Li, L. Cheng, Y. Z. Mao, and D. J. Gz, "The mesoscopic structure of flower-like ZnO nanorods for acetone detection," *Mater. Lett.*, vol. 121, pp. 137–140, 2014.
- [97] H. Haick, Y. Y. Broza, P. Mochalski, V. Ruzsanyi, and A. Amann, "Assessment, origin, and implementation of breath volatile cancer markers," *Chem. Soc. Rev.*, vol. 43, no. 5, pp.

- 1423–49, 2014.
- [98] M. Epifani, E. Comini, R. D??az, T. Andreu, A. Genc, J. Arbiol, P. Siciliano, G. Faglia, and J. R. Morante, “Acetone sensing with TiO₂-WO₃ nanocomposites: An example of response enhancement by inter-oxide cooperative effects,” *Procedia Eng.*, vol. 87, pp. 803–806, 2014.
 - [99] L. Wang, A. Teleki, S. E. Pratsinis, P. I. Gouma, L. Wang, and A. Teleki, “Ferroelectric WO₃ Nanoparticles for Acetone Selective Detection,” *Chem. Mater.*, vol. 20, no. 15, pp. 4794–4796, 2008.
 - [100] M. I. Zaki, M. A. Hasan, F. A. Al-Sagheer, and L. Pasupulety, “Surface Chemistry of Acetone on Metal Oxides: IR Observation of Acetone Adsorption and Consequent Surface Reactions on Silica-Alumina versus Silica and Alumina,” *Langmuir*, vol. 16, pp. 430–436, 2000.
 - [101] N. V. Pavlenko, A. I. Tripol’skii, and G. I. Golodets, “ADSORPTION OF ACETONE AND HYDROGEN ON ALUMINUM OXIDE,” *Theor. Exp. Chem.*, vol. 21, no. 3, pp. 315–319, 1985.
 - [102] H. Zarrin, S. Sy, J. Fu, G. Jiang, K. Kang, Y.-S. Jun, A. Yu, M. Fowler, and Z. Chen, “Molecular Functionalization of Graphene Oxide for Next-Generation Wearable Electronics,” *ACS Appl. Mater. Interfaces*, vol. 8, no. 38, pp. 25428–25437, 2016.
 - [103] G. Jiang, M. Goledzinowski, F. J. E. Comeau, H. Zarrin, G. Lui, J. Lenos, A. Veileux, G. Liu, J. Zhang, S. Hemmati, J. Qiao, and Z. Chen, “Free-Standing Functionalized Graphene Oxide Solid Electrolytes in Electrochemical Gas Sensors,” *Adv. Funct. Mater.*, vol. 26, no. 11, pp. 1729–1736, 2016.
 - [104] National Institute of Standards and Technology, *NIST Chemistry WebBook, SRD 69*. 2017.

Appendices

Appendix A: Estimation of Analyte Vapour Concentration with Henry's Law

All vapour phase concentrations were calculated based on the following temperature dependent equation [104]:

$$k_H = k_H^o \exp \left(C \left(\frac{1}{T} - \frac{1}{298.15} \right) \right) [bar]$$

Where,

k_H = the analyte vapour pressure at temperature T

k_H^o = the analyte vapour pressure at 298.15 K, $\frac{mol}{kg \text{ bar}}$

T = temperature in Kevlin

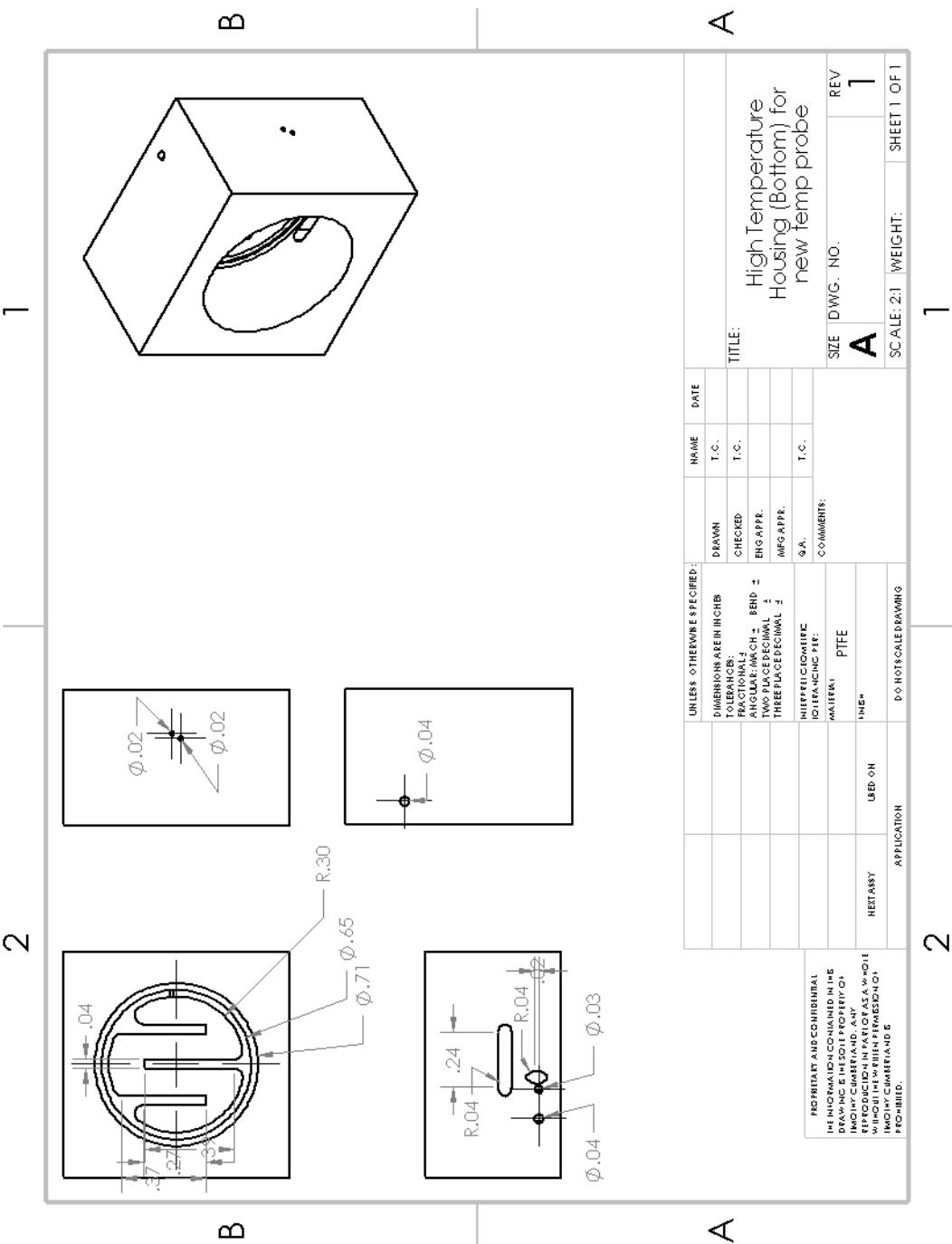
$C = \frac{\ln(k_H)}{d\left(\frac{1}{T}\right)}$, a temperature dependent constant, experimentally obtained

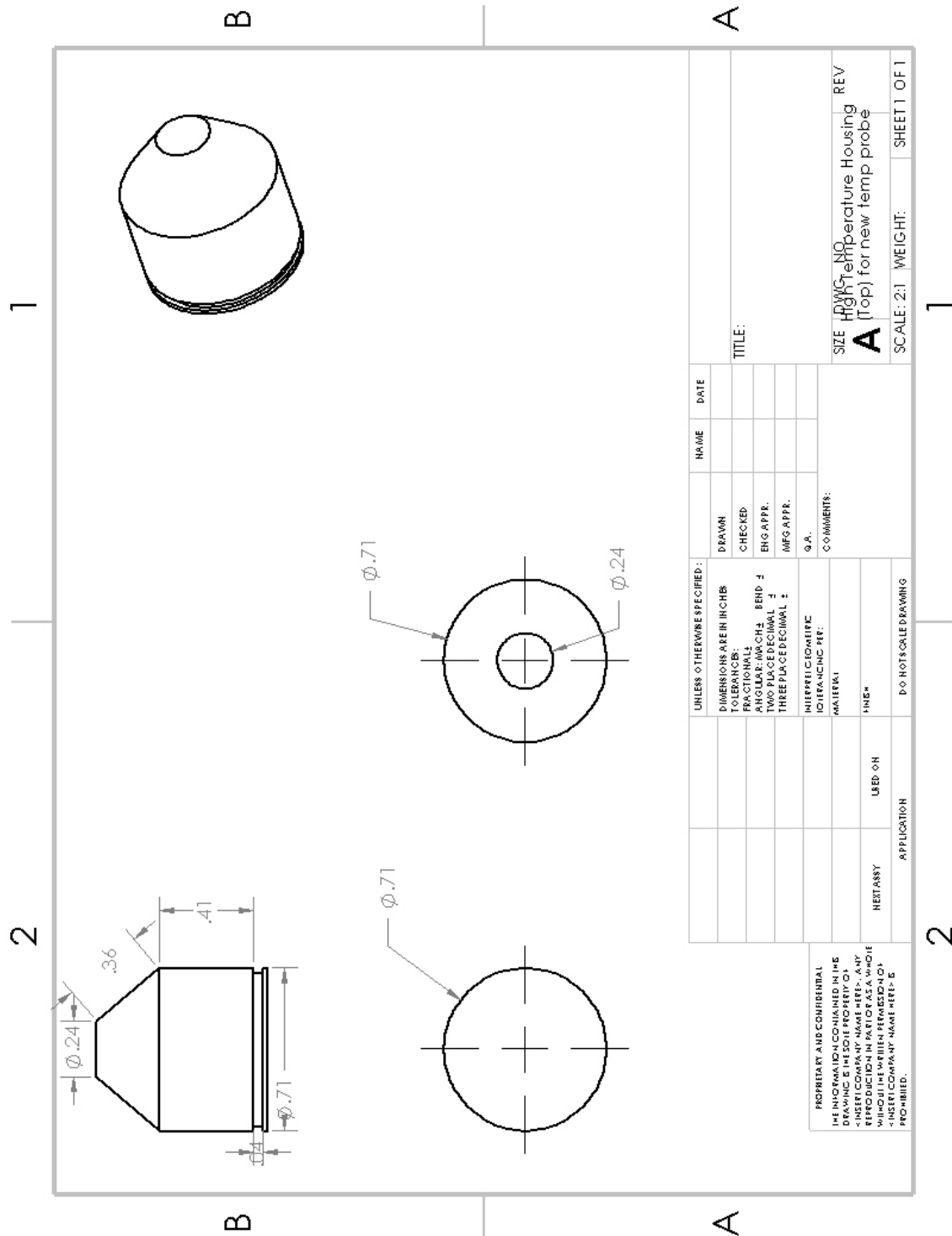
For acetone, the k_H^o and C were given as $27 \frac{mol}{kg \text{ bar}}$ and 5300 K respectively. With a diluted acetone solution at 0.08% v/v and 34°C, the equation yielded a k_H value of 6.7×10^{-4} bar. To convert this partial pressure value to ppmv, the relationship between volume and mol was applied through Dalton's law under the assumption of ideal gas. The equation is as followed:

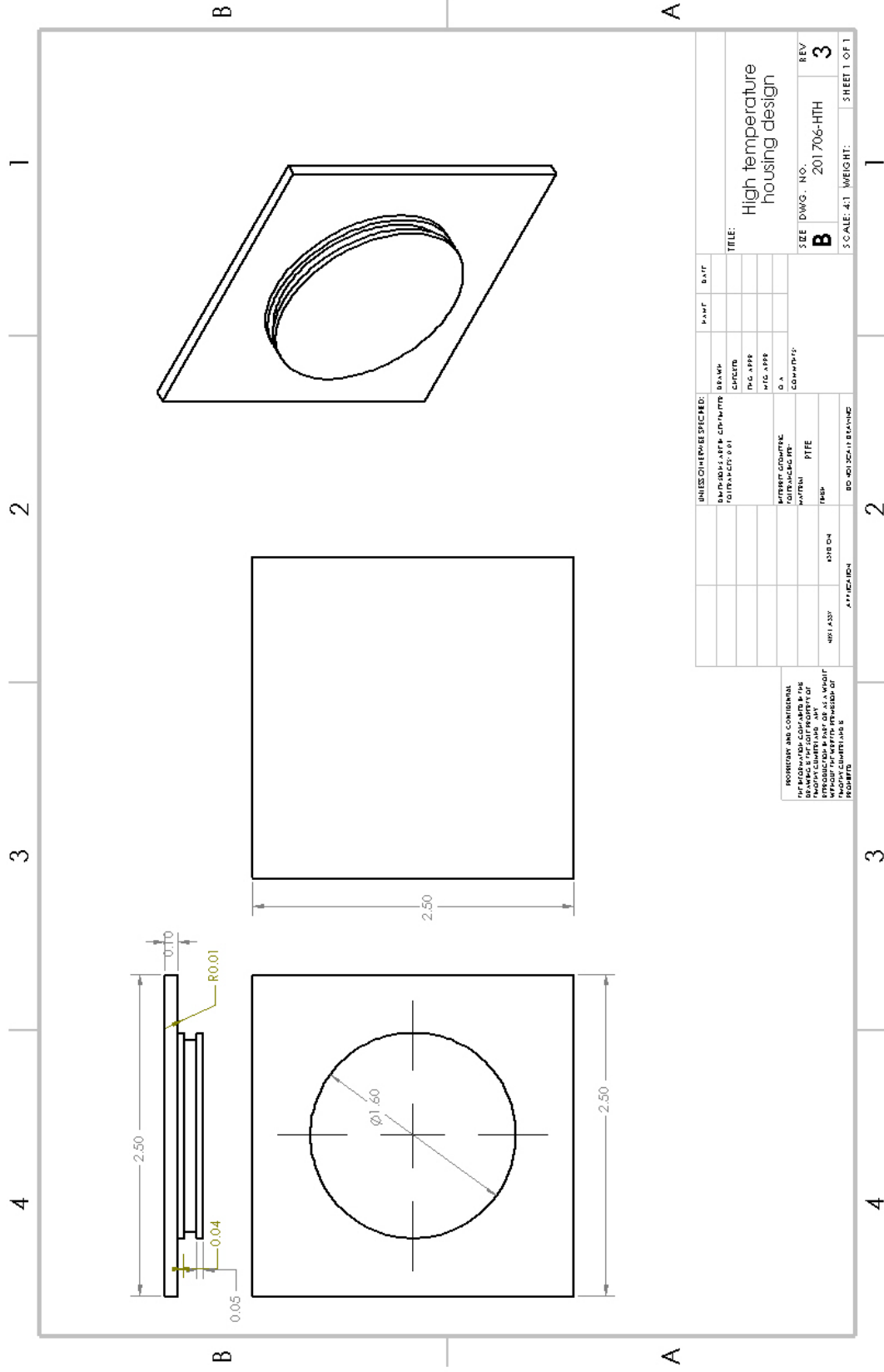
$$P_{partial} = \frac{analyte \text{ ppmv}}{1000000 \text{ ppmv}} * total \text{ pressure}$$

Here, P_{partial} is and total pressure is 1 atm. Thus, a 0.08%v/v acetone/DI solution at 34°C will yield a vapour concentration of 669.9ppmv. This value was compared with another source [70]. This source used a different equation and yielded an acetone ppmv value of 705.2 ppmv.

Appendix B: Fuel Cell Sensor Housing Design Drawing







UNLESS OTHERWISE SPECIFIED:				DATE	
BRASS	BRASS	BRASS	BRASS	DATE	DATE
CLIPPER	CLIPPER	CLIPPER	CLIPPER	DATE	DATE
PLC APPR	PLC APPR	PLC APPR	PLC APPR	DATE	DATE
WTC APPR	WTC APPR	WTC APPR	WTC APPR	DATE	DATE
Q.A.	Q.A.	Q.A.	Q.A.	DATE	DATE
BATTERY COUNTER				DATE	
THERMAL PROTECTION				DATE	
MATERIAL				DATE	
PASTE				DATE	
APPROVAL				DATE	
BY: [Signature]				DATE	
FOR: [Signature]				DATE	
BY: [Signature]				DATE	
FOR: [Signature]				DATE	
BY: [Signature]				DATE	
FOR: [Signature]				DATE	
BY: [Signature]				DATE	
FOR: [Signature]				DATE	
BY: [Signature]				DATE	
FOR: [Signature]				DATE	
BY: [Signature]				DATE	
FOR: [Signature]				DATE	
BY: [Signature]				DATE	
FOR: [Signature]				DATE	
BY: [Signature]				DATE	
FOR: [Signature]				DATE	
BY: [Signature]				DATE	
FOR: [Signature]				DATE	
BY: [Signature]				DATE	
FOR: [Signature]				DATE	
BY: [Signature]				DATE	
FOR: [Signature]				DATE	
BY: [Signature]				DATE	
FOR: [Signature]				DATE	
BY: [Signature]				DATE	
FOR: [Signature]				DATE	
BY: [Signature]				DATE	
FOR: [Signature]				DATE	
BY: [Signature]				DATE	
FOR: [Signature]				DATE	
BY: [Signature]				DATE	
FOR: [Signature]				DATE	
BY: [Signature]				DATE	
FOR: [Signature]				DATE	
BY: [Signature]				DATE	
FOR: [Signature]				DATE	
BY: [Signature]				DATE	
FOR: [Signature]				DATE	
BY: [Signature]				DATE	
FOR: [Signature]				DATE	
BY: [Signature]				DATE	
FOR: [Signature]				DATE	
BY: [Signature]				DATE	
FOR: [Signature]				DATE	
BY: [Signature]				DATE	
FOR: [Signature]				DATE	
BY: [Signature]				DATE	
FOR: [Signature]				DATE	
BY: [Signature]				DATE	
FOR: [Signature]				DATE	
BY: [Signature]				DATE	
FOR: [Signature]				DATE	
BY: [Signature]				DATE	
FOR: [Signature]				DATE	
BY: [Signature]				DATE	
FOR: [Signature]				DATE	
BY: [Signature]				DATE	
FOR: [Signature]				DATE	
BY: [Signature]				DATE	
FOR: [Signature]				DATE	
BY: [Signature]				DATE	
FOR: [Signature]				DATE	
BY: [Signature]				DATE	
FOR: [Signature]				DATE	
BY: [Signature]				DATE	
FOR: [Signature]				DATE	
BY: [Signature]				DATE	
FOR: [Signature]				DATE	
BY: [Signature]				DATE	
FOR: [Signature]				DATE	
BY: [Signature]				DATE	
FOR: [Signature]				DATE	
BY: [Signature]				DATE	
FOR: [Signature]				DATE	
BY: [Signature]				DATE	
FOR: [Signature]				DATE	
BY: [Signature]				DATE	
FOR: [Signature]				DATE	
BY: [Signature]				DATE	
FOR: [Signature]				DATE	
BY: [Signature]				DATE	
FOR: [Signature]				DATE	
BY: [Signature]				DATE	
FOR: [Signature]				DATE	
BY: [Signature]				DATE	
FOR: [Signature]				DATE	
BY: [Signature]				DATE	
FOR: [Signature]				DATE	
BY: [Signature]				DATE	
FOR: [Signature]				DATE	
BY: [Signature]				DATE	
FOR: [Signature]				DATE	
BY: [Signature]				DATE	
FOR: [Signature]				DATE	
BY: [Signature]				DATE	
FOR: [Signature]				DATE	
BY: [Signature]				DATE	
FOR: [Signature]				DATE	
BY: [Signature]				DATE	
FOR: [Signature]				DATE	
BY: [Signature]				DATE	
FOR: [Signature]				DATE	
BY: [Signature]				DATE	
FOR: [Signature]				DATE	
BY: [Signature]				DATE	
FOR: [Signature]				DATE	
BY: [Signature]				DATE	
FOR: [Signature]				DATE	
BY: [Signature]				DATE	
FOR: [Signature]				DATE	
BY: [Signature]				DATE	
FOR: [Signature]				DATE	
BY: [Signature]				DATE	
FOR: [Signature]				DATE	
BY: [Signature]				DATE	
FOR: [Signature]				DATE	
BY: [Signature]				DATE	
FOR: [Signature]				DATE	
BY: [Signature]				DATE	
FOR: [Signature]				DATE	
BY: [Signature]				DATE	
FOR: [Signature]				DATE	
BY: [Signature]				DATE	
FOR: [Signature]				DATE	
BY: [Signature]				DATE	
FOR: [Signature]				DATE	
BY: [Signature]				DATE	
FOR: [Signature]				DATE	
BY: [Signature]				DATE	
FOR: [Signature]				DATE	
BY: [Signature]				DATE	
FOR: [Signature]				DATE	
BY: [Signature]				DATE	
FOR: [Signature]				DATE	
BY: [Signature]				DATE	
FOR: [Signature]				DATE	
BY: [Signature]				DATE	
FOR: [Signature]				DATE	
BY: [Signature]				DATE	
FOR: [Signature]				DATE	
BY: [Signature]				DATE	
FOR: [Signature]				DATE	
BY: [Signature]				DATE	
FOR: [Signature]				DATE	
BY: [Signature]				DATE	
FOR: [Signature]				DATE	
BY: [Signature]				DATE	
FOR: [Signature]				DATE	
BY: [Signature]				DATE	
FOR: [Signature]				DATE	
BY: [Signature]				DATE	
FOR: [Signature]				DATE	
BY: [Signature]				DATE	
FOR: [Signature]				DATE	
BY: [Signature]				DATE	
FOR: [Signature]				DATE	

Appendix C: Test Automation and Data Analysis Code

DMM Controller and Data Acquisition

SCREEN SHOT OF BENCHVUE TEST FLOW

Hardware Control Script

Batch file to go into the BenchVue TestFlow

```
cd Desktop
REM the directory can be altered to any directory user place the replywrite.py file
python relaywrite.py
```

Python script called by the Batch file to control the two pumps

```
#SENSOR TEST SYSTEM CONTROLLER

#Python3 script to control a NumatoLab 2-relay module
#This script was specifically made to operate an air pump and a sample pump at fix intervals to
creat reliable replication of each sensor test
#This script can be used within the BenchVue's TestFlow through a bash file or run independently

#Dependency: pyserial. MUST be installed with for Python to have access to the COM ports

#Created by: Timothy Cumberland
#Email: tdkcumberland@gmail.com
#Last Eddited: June 21,2018

import serial
from time import sleep

portName = "COM2" #prior to running, check DeviceManager to confirm the port number
relayNum0 = 0
relayNum1 = 1
relayCmdon = "on"
relayCmdoff = "off"
#*-Open port for communication-*-#
serPort = serial.Serial(portName, 19200, timeout=1)

#*-Sending command to the the appropriate relay-*-#
#Turning air pump relay on
commandline = "relay "+ str(relayCmdon) +" "+ str(relayNum0) + "\n\r"
serPort.write(commandline.encode())

sleep(3) #wait for 3 seconds, can be adjusted

#turning sampling pump on
commandline = "relay "+ str(relayCmdon) +" "+ str(relayNum1) + "\n\r"
serPort.write(commandline.encode())

sleep(2) #wait for 2 seconds, can be adjusted, WARNING: leaving the sampling pump on for too long
may damage the pump

#turn both pumps off
commandline = "relay "+ str(relayCmdoff) +" "+ str(relayNum0) + "\n\r"
serPort.write(commandline.encode())
commandline = "relay "+ str(relayCmdoff) +" "+ str(relayNum1) + "\n\r"
```

```
serPort.write(commandline.encode())

#*-Close the port-*-#
serPort.close()
```

Sensor Response Curve Batch Process

#AUTOMATIC BATCH PROCESS SCRIPT FOR ACETONE GAS SENSOR RESPONSE

```
#This script extracts the sensor response data from the CSV files output by the KeySight DMM
BenchVue Software.
#The script is capable of process all the CSV files in a batch mode within a specified directory.
#NOTE: the user should have administrative level previlige when running this script since there
is read and write procedure that may requires such permission
#Python version: 3.6.6rc1
#Dependencies: Scipy stack

#Created by: Timothy Cumberland
#Email: tdkcumberland@gmail.com
#Last edited: June 22, 2018
```

```
import os
import numpy as np
import pandas as pd
import matplotlib.pyplot as plt
```

```
def find_nearest(array, value): #this function seeks and finds a user defined value closest to
value within a specified array
    array = np.asarray(array)
    idx = (np.abs(array - value)).argmin()
    return array[idx]
```

```
data_list = [] #initialize an array to hold the results to be later appended to a dataframe
```

```
directory=("C:\\Users\\Timothy Kim\\Desktop\\Python Test") #user can specify the directory
containing the CSV files
```

```
for root,dirs,files in os.walk(directory):
    for file in files:
```

```
        newdirectory = os.path.join(directory,file)
        newdata = pd.read_csv(newdirectory, sep=',', header = 5, names = ["SamplerNumber",
"Time", "Data", "Empty"], infer_datetime_format=True)
        #--data preprocessing--#
        newdata.Data = newdata.Data*1e6 #convert the current response to from nA to uA
```

```
        newdata['Time'] = pd.to_datetime(newdata['Time']) #format time stamp to total second
elapsed
        newdata['Time'] = newdata['Time'] - newdata['Time'][0]
        newdata['Time'] = newdata['Time'].dt.total_seconds()
```

```
        #newdata.plot(x="Time",y="Data") #user can use this code segment to graph the resonse
curve
        #plt.show()
```

```
        #--data analysis--#
        peak_value = max(newdata.Data) #find peak value and its index
        peak_index = newdata.index[newdata['Data'] == peak_value].tolist()
```

```
        tempdata = newdata['Data'][peak_index[0]:-1] # create a temporary data set starting from
the peak till end
```

```
        three_8th_peak = 3/8*peak_value #find 3/4 and 3/8 peak values and their indexes
        three_4th_peak = 3/4*peak_value
        three_8th_peak = find_nearest(tempdata, three_8th_peak)
        three_4th_peak = find_nearest(tempdata, three_4th_peak)
```

```
        three_8th_peak_index = tempdata.index[tempdata == three_8th_peak].tolist()
        three_4th_peak_index = tempdata.index[tempdata == three_4th_peak].tolist()
```



```

        #calculate the 3/8 and 3/4 area
        three_8th_area = np.trapz(y = np.asarray(newdata['Data'][:three_8th_peak_index[0]]), x =
np.asarray(newdata['Time'][:three_8th_peak_index[0]]))
        three_4th_area = np.trapz(y = np.asarray(newdata['Data'][:three_4th_peak_index[0]]), x =
np.asarray(newdata['Time'][:three_4th_peak_index[0]]))

        #calculate total area
        total_area = three_4th_area + 2*(three_8th_area - three_4th_area)
        #print([three_8th_area, three_4th_area, total_area])
        data_list.append([peak_value,total_area])

output_df = pd.DataFrame(data_list, columns = ['Peak (uA)','Area (uA s)' ]) #output the results
into a dataframe with properly formatted column headings
output_df.to_csv(directory, sep = '\t') #the output results are exported into a new CSV file
within the same directory

```